

Nonheme Fe(IV) Oxo Complexes of Two New Pentadentate Ligands and Their Hydrogen-Atom and Oxygen-Atom Transfer Reactions

Mainak Mitra,[†] Hassan Nimir,[‡] Serhiy Demeshko,[§] Satish S. Bhat,[†] Sergey O. Malinkin,[†] Matti Haukka,[⊥] Julio Lloret-Fillol,[¶] George C. Lisensky,^{||} Franc Meyer,[§] Albert A. Shteinman,[#] Wesley R. Browne,[∇] David A. Hrovat,[○] Michael G. Richmond,[◆] Miquel Costas,[¶] and Ebbe Nordlander^{*†}

[†]Chemical Physics, Department of Chemistry, Lund University, Box 124, SE-221 00, Lund, Sweden

[‡]Department of Chemistry and Earth Sciences, College of Arts and Sciences, Qatar University, P.O. Box 2713, Doha, State of Qatar

[§]Institute of Inorganic Chemistry, Georg-August-University Göttingen, Tammanstrasse 4, D-37077 Göttingen, Germany

^{||}Department of Chemistry, Beloit College, 700 College Street, Beloit, Wisconsin 53511, United States

[⊥]Department of Chemistry, University of Jyväskylä, P.O. Box-35, Jyväskylä, FI-40014, Finland

[#]Institute of Problems of Chemical Physics, Chernogolovka, Moscow District, 142432, Russian Federation

[∇]Stratingh Institute for Chemistry, Faculty of Mathematics and Natural Sciences, University of Groningen, Nijenborgh 4, 9747AG Groningen, The Netherlands

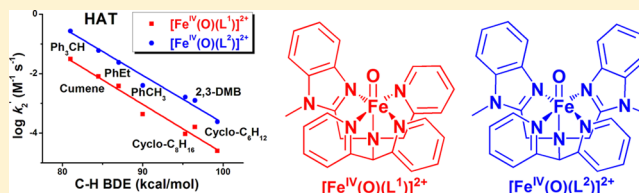
[○]Center for Advanced Scientific Computing and Modeling, University of North Texas, Denton, Texas 76203, United States

[◆]Department of Chemistry, University of North Texas, Denton, Texas 76203, United States

[¶]QBIS, Department of Chemistry, University de Girona, Campus Montilivi, E-17071 Girona, Spain

Supporting Information

ABSTRACT: Two new pentadentate {NS} donor ligands based on the N4Py (N4Py = *N,N*-bis(2-pyridylmethyl)-*N*-bis(2-pyridyl)methylamine) framework have been synthesized, viz. [*N*-(1-methyl-2-benzimidazolyl)methyl-*N*-(2-pyridyl)methyl-*N*-(bis-2-pyridyl methyl)amine] (L¹) and [*N*-bis(1-methyl-2-benzimidazolyl)methyl-*N*-(bis-2-pyridylmethyl)amine] (L²), where one or two pyridyl arms of N4Py have been replaced by corresponding (*N*-methyl)benzimidazolyl-containing arms. The complexes [Fe^{II}(CH₃CN)(L)]²⁺ (L = L¹ (1); L² (2)) were synthesized, and reaction of these ferrous complexes with iodossylbenzene led to the formation of the ferryl complexes [Fe^{IV}(O)(L)]²⁺ (L = L¹ (3); L² (4)), which were characterized by UV–vis spectroscopy, high resolution mass spectrometry, and Mössbauer spectroscopy. Complexes 3 and 4 are relatively stable with half-lives at room temperature of 40 h (L = L¹) and 2.5 h (L = L²). The redox potentials of 1 and 2, as well as the visible spectra of 3 and 4, indicate that the ligand field weakens as ligand pyridyl substituents are progressively substituted by (*N*-methyl)benzimidazolyl moieties. The reactivities of 3 and 4 in hydrogen-atom transfer (HAT) and oxygen-atom transfer (OAT) reactions show that both complexes exhibit enhanced reactivities when compared to the analogous N4Py complex ([Fe^{IV}(O)(N4Py)]²⁺), and that the normalized HAT rates increase by approximately 1 order of magnitude for each replacement of a pyridyl moiety; i.e., [Fe^{IV}(O)(L²)]²⁺ exhibits the highest rates. The second-order HAT rate constants can be directly related to the substrate C–H bond dissociation energies. Computational modeling of the HAT reactions indicates that the reaction proceeds via a high spin transition state.



INTRODUCTION

High valent Fe(IV) oxo species have been established as key oxidizing intermediates in the activation of molecular oxygen in many iron-containing enzymes.^{1–3} For example, nonheme high spin (*S* = 2) Fe(IV) oxo intermediates have been identified as active oxidizing species in the catalytic cycles of *E. coli* taurine:α-ketoglutaratedioxygenase (TauD),⁴ propyl-4-hydroxylase,⁵ halogenase CytC3,⁶ tyrosine hydroxylase,⁷ and the aliphatic halogenase SyrB2⁸ by means of various spectroscopic techniques. These reactive intermediates functionalize C–H

bonds in a wide number of substrates, transforming them into hydroxylated, unsaturated, or halogenated products.^{4b,5–7,9}

The interesting chemistry that is exhibited by nonheme iron enzymes has inspired extensive efforts to mimic their high valent intermediates and emulate their reactivities.^{2,10} Over the past decade, several nonheme Fe(IV) oxo (ferryl) complexes supported by a wide range of pentadentate and tetradentate ligands have been prepared.^{2,10,11} These Fe(IV) oxo complexes

Received: December 10, 2014

have been investigated for, *inter alia*, hydrogen-atom transfer and oxygen-atom transfer reactions, and the reactivities of these different nonheme Fe(IV) oxo complexes have been found to vary widely. For example, $[\text{Fe}^{\text{IV}}(\text{O})(\text{TMC})(\text{NCMe})]^{2+}$ (TMC = 1,4,8,11-tetramethyl-1,4,8,11-tetraazacyclotetradecane) can only oxidize substrates with C–H bond dissociation energies (BDE) of <80 kcal/mol,¹² while $[\text{Fe}^{\text{IV}}(\text{O})(\text{N4Py})]^{2+}$ (N4Py = *N,N*-bis(2-pyridylmethyl)-*N,N'*-bis(2-pyridyl)methylamine) and $[\text{Fe}^{\text{IV}}(\text{O})(\text{Bn-tpen})]^{2+}$ (Bn-tpen = *N*-benzyl-*N,N',N'*-tris(2-pyridylmethyl)-1,2-diaminoethane) (Figure 1) have been shown to oxidize strong C–H bonds, *e.g.*, those in cyclohexane (C–H BDE 99.3 kcal/mol) at room temperature.¹³

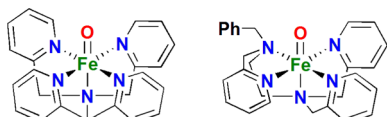


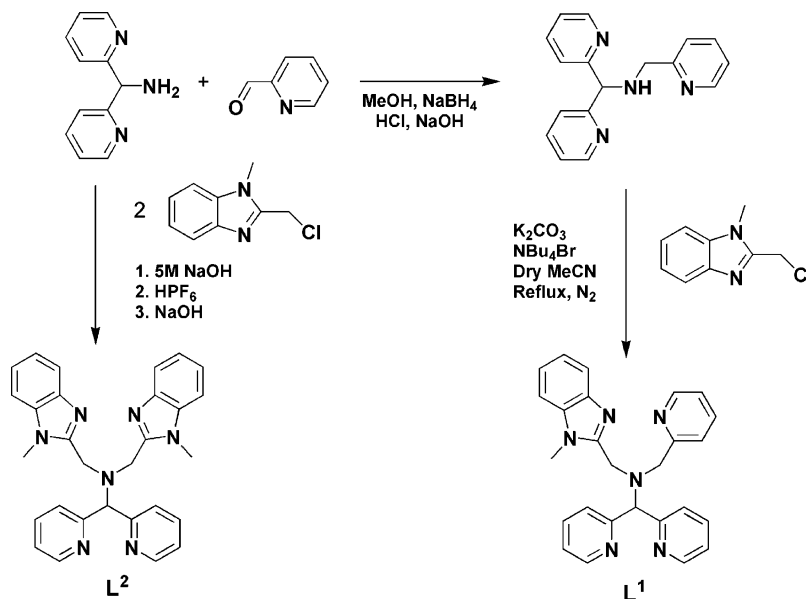
Figure 1. Two nonheme Fe(IV) oxo complexes: $[\text{Fe}^{\text{IV}}(\text{O})(\text{N4Py})]^{2+}$ (left) and $[\text{Fe}^{\text{IV}}(\text{O})(\text{Bn-tpen})]^{2+}$ (right).

The spin state on the iron center of the Fe(IV) oxo unit has been proposed to play a crucial role in terms of reactivity. It has been predicted theoretically that the high spin ($S = 2$) Fe(IV) oxo complexes are more reactive than low spin ($S = 1$) Fe(IV) oxo complexes (*vide infra*).^{11,14,15} A significant aspect of the observed reactivities and spin states of ferryl complexes is that they can be modulated by the various ligand environments supporting the Fe(IV) oxo unit. A high spin ($S = 2$) Fe(IV) oxo unit may be achieved by adopting a trigonal bipyramidal (TBP) geometry using tetradentate ligands with sufficient steric constraints, as observed in the case of $[\text{Fe}^{\text{IV}}(\text{O})(\text{TMG}_3\text{tren})]^{2+}$ (TMG₃tren = tris(tetramethylguanidino)tren)¹⁶ and $[\text{Fe}^{\text{IV}}(\text{O})(\text{H}_3\text{buea})]^-$ (H₃buea = tris(*tert*-butylureaylethylene)aminato)¹⁷ leading to degeneracy of the second highest occupied molecular orbitals, which have significant d_{xy} and $d_{x^2-y^2}$ character. A detailed investigation was recently made on five low spin Fe(IV) oxo complexes comprising pentadentate pyridine- and amine-based ligands to examine the correlation of the rates of

hydrogen-atom transfer and oxygen-atom transfer processes with their spectroscopic and electrochemical properties which are controlled by the ligand scaffold.¹⁸ The oxo transfer process to thioanisole by these five Fe(IV) oxo complexes has been correlated to the redox potential of the Fe(IV)/Fe(III) couple which was influenced by the ligands bound to the Fe-oxo unit; however, such a direct correlation could not be concluded in the case of hydrogen abstraction processes.¹⁸ Due to the relative dearth of high spin Fe^{IV}=O complexes, the reactivity of this class of complexes is less well-explored.¹¹ It has been shown that such complexes can undergo hydrogen-atom transfer (HAT) reactions, but in general with relatively low reaction rates in comparison with the most reactive low spin Fe^{IV}=O complexes.^{19,20} Recently, one high spin Fe^{IV}=O complex, $[\text{Fe}^{\text{IV}}(\text{O})(\text{TQA})(\text{NCMe})]^{2+}$ (TQA = tris(2-quinolylmethyl)amine), was found to be significantly more reactive toward HAT than other $S = 2$ Fe^{IV}=O complexes, and was also found to effect alkene epoxidation.²¹

We wish to investigate whether the reactivity of ferryl complexes can be tuned by modification of the steric and electronic properties of ligands, and whether the reactivity of such complexes can be improved while maintaining thermal stability. For this purpose, we chose to modify/derivatize the N4Py ligand framework.²² Among bioinspired Fe^{IV}=O complexes, $[\text{Fe}^{\text{IV}}(\text{O})(\text{N4Py})]^{2+}$ has been shown to exhibit the unique combination of powerful oxidative reactivity toward alkanes, enabling it to cleave strong C–H bonds, while at the same time possessing considerable thermal stability; indeed, the stability has been proven sufficient to permit its structure to be characterized by X-ray crystallography.²³ A number of modifications of the N4Py ligand framework have been made,^{24,25} but they do not include the replacement of the pyridyl moieties of this ligand with other nitrogen donor moieties. We were therefore interested in attempting to modify the stability and reactivity of N4Py by tuning the ligand coordination environment, and we chose to introduce (*N*-methyl)benzimidazolyl moieties as these are relatively close analogues of histidine imidazolyls. Although there are a few examples of benzimidazolyl donors exerting profound influence

Scheme 1. Schematic Synthetic Routes for Ligands L¹ and L²



on the reactivities of bioinspired nonheme iron catalysts in oxidation,^{15,26,27} there is only one previous study involving the coordination of such donor moieties to an isolated/detected/identified $\text{Fe}^{\text{IV}}=\text{O}$ complex.¹⁵ The five-coordinate complex $[\text{Fe}^{\text{II}}(\text{Me}_3\text{NTB})(\text{NCMe})](\text{OTf})_2$ (Me_3NTB = tris(*N*-methylbenzimidazol-2-yl)methyl)amine), the (*N*-methyl)benzimidazolyl equivalent of the tripodal tris(2-pyridylmethyl)amine (TPA) ligand, reacts with *m*-CPBA at -40 °C to form the very reactive ($S = 1$) $[\text{Fe}^{\text{IV}}(\text{O})(\text{Me}_3\text{NTB})]^{2+}$ complex, which is proposed to be more reactive than Cyt P450 model compound I ($[\text{Fe}^{\text{IV}}(\text{O})(\text{TDCPP})]^{2+}$, TDCPP = *meso*-tetrakis-(2,6-dichlorophenyl)porphinatodianion).¹⁵ However, this ferryl species with a solvent acting as a sixth ligand and with a plausible pseudo-octahedral coordination geometry around the iron is unstable and decays fast even at -40 °C ($t_{1/2} = 2$ min).

The two new pentadentate ligands L^1 and L^2 that have been prepared are thus based on the N4Py ligand framework, with one (L^1) or two (L^2) of the (2-pyridyl)methyl arms of N4Py being exchanged by one (or two) (*N*-methylbenzimidazolyl)-methyl arm(s). The (*N*-methyl)benzimidazole moiety contains not only greater steric bulk but is generally considered to be a better σ -donor than the pyridine moiety.²⁸ It has recently been shown that such a simple change of a ligand donor moiety can affect the catalytic activities of Fe(II) complexes in alkane and alkene oxidation reactions,²⁷ and it was envisioned that the chemistry of high valent Fe(IV) oxo species, e.g., $[\text{Fe}^{\text{IV}}(\text{O})(\text{N4Py})]^{2+}$, may also be sensitive to such a change. Here we report two new Fe(II) complexes based on the two ligands, the generation and characterization of their corresponding Fe(IV) oxo complexes, and the reactivities of their ferryl species toward hydrogen-atom transfer and oxygen-atom transfer processes.

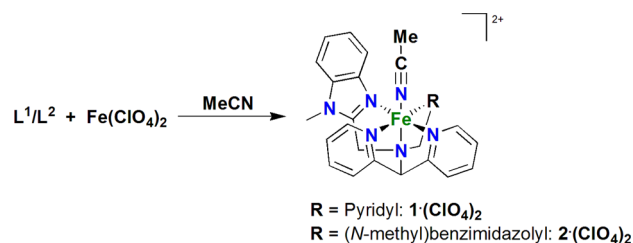
RESULTS AND DISCUSSION

Synthesis and Characterization of Ligands and Complexes. Ligand L^1 was synthesized by reaction of *N*-[di(2-pyridyl)methyl]-*N*-(2-pyridylmethyl)methylamine²⁹ with 1 equiv of 2-chloromethyl-1-methylbenzimidazole in refluxing dry acetonitrile, in the presence of K_2CO_3 and tetrabutylammonium bromide (Scheme 1). Ligand L^2 was synthesized by reaction of bis(2-pyridyl)methylamine³⁰ with 2 equiv of 2-chloromethyl-1-methylbenzimidazole in the presence of aqueous NaOH solution (Scheme 1).

The corresponding Fe(II) complexes, $[\text{Fe}^{\text{II}}(\text{CH}_3\text{CN})(\text{L}^1)](\text{ClO}_4)_2$ ($1 \cdot (\text{ClO}_4)_2$) and $[\text{Fe}^{\text{II}}(\text{CH}_3\text{CN})(\text{L}^2)](\text{ClO}_4)_2$ ($2 \cdot (\text{ClO}_4)_2$), were prepared by reaction of 1 equiv of L^1/L^2 with 1 equiv of hydrated $\text{Fe}(\text{ClO}_4)_2$ in a minimum amount of dry acetonitrile solvent at room temperature (Scheme 2). Both complexes $1 \cdot (\text{ClO}_4)_2$ and $2 \cdot (\text{ClO}_4)_2$ were isolated as air-stable solids.

The ESI mass spectrum of $1 \cdot (\text{ClO}_4)_2$ in acetonitrile shows peaks at $m/z = 238$ and $m/z = 258.5$ corresponding to the formulations $[\text{Fe}^{\text{II}}(\text{L}^1)]^{2+}$ (calcd 238) and $[\text{Fe}^{\text{II}}(\text{L}^1)(\text{CH}_3\text{CN})]^{2+}$ (calcd 258.5), respectively, as well as peaks at $m/z = 575.1$ and $m/z = 616.1$ corresponding to the formulations $[\text{Fe}^{\text{II}}(\text{L}^1)(\text{ClO}_4)]^+$ (calcd 575.1) and $[\text{Fe}^{\text{II}}(\text{L}^1)(\text{CH}_3\text{CN})(\text{ClO}_4)]^+$ (calcd 616.1), respectively (Figure S1, Supporting Information). Similarly, the ESI-MS of complex $2 \cdot (\text{ClO}_4)_2$ in acetonitrile shows prominent peaks at $m/z = 264.6$ and $m/z = 628.1$ corresponding to the formulations $[\text{Fe}^{\text{II}}(\text{L}^2)]^{2+}$ (calcd 264.6) and $[\text{Fe}^{\text{II}}(\text{L}^2)(\text{ClO}_4)]^+$ (calcd 628.1), respectively (Figure S2, Supporting Information).

Scheme 2. Synthesis of the Fe(II) Complexes $[\text{Fe}^{\text{II}}(\text{CH}_3\text{CN})(\text{L}^1)](\text{ClO}_4)_2$ ($1 \cdot (\text{ClO}_4)_2$) and $[\text{Fe}^{\text{II}}(\text{CH}_3\text{CN})(\text{L}^2)](\text{ClO}_4)_2$ ($2 \cdot (\text{ClO}_4)_2$)



The UV–vis spectra of the ligands L^1 and L^2 in acetonitrile solution show high intensity bands in the UV region (wavelength < 300 nm) (Figure S3, Supporting Information). Upon coordination to the Fe(II) ion, two new charge transfer (CT) bands appear in the visible region. For complex $1 \cdot (\text{ClO}_4)_2$, the CT bands appear at $\lambda_{\text{max}} = 387$ nm ($\epsilon \approx 5200 \text{ M}^{-1} \text{ cm}^{-1}$) and 466 nm ($\epsilon \approx 4300 \text{ M}^{-1} \text{ cm}^{-1}$), while for complex $2 \cdot (\text{ClO}_4)_2$, the CT bands appear at $\lambda_{\text{max}} = 404$ nm ($\epsilon \approx 3200 \text{ M}^{-1} \text{ cm}^{-1}$) and 477 nm ($\epsilon \approx 2100 \text{ M}^{-1} \text{ cm}^{-1}$) (Figure 2). These CT

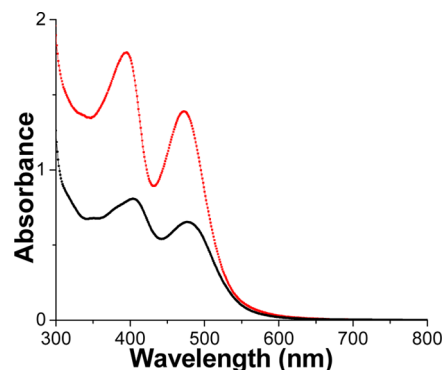


Figure 2. UV–vis spectra of complexes $1 \cdot (\text{ClO}_4)_2$ (red) and $2 \cdot (\text{ClO}_4)_2$ (black) (0.25 mM) in acetonitrile recorded at room temperature (298 K).

bands can be assigned as metal to ligand charge transfer (MLCT) bands arising from electron transfer from low spin Fe(II) t_{2g} orbitals to the π^* orbitals of the ligand. The weaker absorbance/smaller observed extinction coefficients for complex 2 relative to 1 may be explained by the presence of a mixture of high spin and low spin forms of the complex in solution (*vide infra*).

The natural abundance ^{57}Fe Mössbauer spectra of the solid samples of complexes $1 \cdot (\text{ClO}_4)_2$ and $2 \cdot (\text{ClO}_4)_2$ measured at 80 K confirm the presence of low spin Fe(II) ions in both complexes in the solid state (Figure 3). The isomeric shift

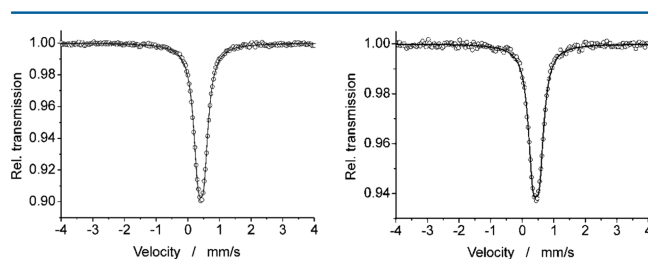


Figure 3. Zero-field Mössbauer spectra of complexes $1 \cdot (\text{ClO}_4)_2$ (left) and $2 \cdot (\text{ClO}_4)_2$ (right) collected at 80 K.

values (δ) and quadrupole splitting values (ΔE_Q) are listed in Table 1. Single-point DFT energy calculations on the $S = 0$, $S =$

Table 1. Mössbauer Parameters for Complexes $1 \cdot (\text{ClO}_4)_2$ and $2 \cdot (\text{ClO}_4)_2$

complex	isomeric shift value (δ) in mm s^{-1}	quadrupole splitting value (ΔE_Q) in mm s^{-1}
$1 \cdot (\text{ClO}_4)_2$	0.41	0.19
$2 \cdot (\text{ClO}_4)_2$	0.44	0.21

1, and $S = 2$ spin states of $1 \cdot (\text{ClO}_4)_2$ and $2 \cdot (\text{ClO}_4)_2$ using the structures obtained from the X-ray diffraction data confirm the $S = 0$ spin state as the ground state of each complex.

Magnetic moment measurements performed on solid samples of $1 \cdot (\text{ClO}_4)_2$ and $2 \cdot (\text{ClO}_4)_2$ show that both complexes remain low spin in the solid state within the temperature range 0–300 K (Figures S4–5, Supporting Information). The ^1H NMR spectrum of $1 \cdot (\text{ClO}_4)_2$ in CD_3CN indicates the presence of a low spin Fe(II) center in solution at room temperature (Figure S6, Supporting Information). However, the ^1H NMR spectrum of complex $2 \cdot (\text{ClO}_4)_2$ in CD_3CN measured at 298 K shows a presence of the high spin form of $2 \cdot (\text{ClO}_4)_2$ as a minor component in solution, in equilibrium with the diamagnetic low spin form (Figure S7, Supporting Information). The variable temperature NMR measurement (VT-NMR) in the temperature range 298–243 K on $2 \cdot (\text{ClO}_4)_2$ in CD_3CN reveals that the high spin Fe(II) center becomes low spin with a decrease in temperature (Figure S8, Supporting Information). The different behaviors of $2 \cdot (\text{ClO}_4)_2$ in the solid state and in solution can explain the observed low intensity in the absorbance value of $2 \cdot (\text{ClO}_4)_2$ relative to $1 \cdot (\text{ClO}_4)_2$ (Figure 2) and implies that the successive introduction of (*N*-methyl)benzimidazolyl moieties into the N4Py ligand framework gradually weakens the ligand-field strength. Thus, there is an increase of the absorbance value of the UV–vis spectrum of complex $2 \cdot (\text{ClO}_4)_2$ in acetonitrile solution when the temperature is lowered from room temperature (298 K) to 243 K (Figure S9, Supporting Information). This may be rationalized by an increased population of the low spin state, with the spectral properties of this state predominating over the transitions connected with the high spin state.

Electrochemistry of Complexes $1 \cdot (\text{ClO}_4)_2$ and $2 \cdot (\text{ClO}_4)_2$. The cyclic voltammograms of complexes $1 \cdot (\text{ClO}_4)_2$ and $2 \cdot (\text{ClO}_4)_2$ were measured in acetonitrile at 298 K using a glassy carbon electrode as the working electrode and SCE as the reference electrode. All potentials are reported versus the ferrocene/ferrocenium potential (0.4 V vs NHE) as an internal standard. Complex $1 \cdot (\text{ClO}_4)_2$ showed a reversible oxidation wave at $E_{1/2} = 0.467$ V, and complex $2 \cdot (\text{ClO}_4)_2$ showed a quasireversible oxidation wave at $E_{1/2} = 0.398$ V (Figure S12, Supporting Information). Peak separations for both these $\text{Fe}^{\text{III}}/\text{Fe}^{\text{II}}$ couples are similar to that of ferrocene. A small impurity of the aquo complex³¹ was also observed at 0.1 V for $1 \cdot (\text{ClO}_4)_2$ and at 0.2 V for $2 \cdot (\text{ClO}_4)_2$. The $[\text{Fe}^{\text{II}}(\text{CH}_3\text{CN})(\text{N4Py})](\text{ClO}_4)_2$ complex has a relatively high redox potential value (1.01 V vs SCE or 0.85 V vs ferrocene).^{25,31} Successive replacement of the pyridyl moieties in N4Py by (*N*-methyl)benzimidazolyl moieties led to an incremental lowering of the oxidation potential in agreement with the benzimidazolyl groups being better σ -donors, thus increasing the electron density on the metal relative to the N4Py complex. Because NMR spectroscopy shows that complex $2 \cdot (\text{ClO}_4)_2$ changes

from high spin to low spin in acetonitrile solution as the solution is cooled, the electrochemistry of $2 \cdot (\text{ClO}_4)_2$ was also measured as a function of temperature. A small shift of 0.07 V to a lower potential was observed as the sample was cooled from 21 to -40 °C (Figure S13, Supporting Information).

Crystal and Molecular Structures of $1 \cdot (\text{ClO}_4)_2$ and $2 \cdot (\text{ClO}_4)_2$. Single crystals suitable for X-ray diffraction were grown for both $1 \cdot (\text{ClO}_4)_2$ and $2 \cdot (\text{ClO}_4)_2$, and their crystal structures were determined in order to confirm the proposed molecular structures. The structures of the two cationic complexes are shown in Figure 4; selected bond distances are collated in Table

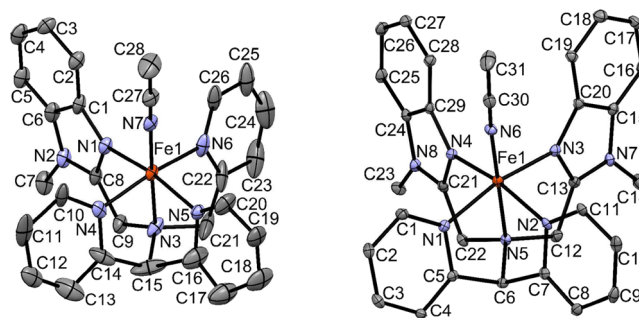


Figure 4. ORTEP plots of the molecular structures of the cations of $1 \cdot (\text{ClO}_4)_2$ (left) and $2 \cdot (\text{ClO}_4)_2$ (right), showing the atom labeling scheme. Thermal ellipsoids are plotted at 30% probability ellipsoids; hydrogen atoms have been omitted for clarity.

Table 2. Selected Bond Distances (Å) for Complexes $1 \cdot (\text{ClO}_4)_2$ and $2 \cdot (\text{ClO}_4)_2$

	$1 \cdot (\text{ClO}_4)_2$	$2 \cdot (\text{ClO}_4)_2$	
Fe(1)–N(7)	1.909(6)	Fe(1)–N(6)	1.901(3)
Fe(1)–N(4)	1.948(6)	Fe(1)–N(1)	1.964(3)
Fe(1)–N(5)	1.957(6)	Fe(1)–N(4)	1.979(2)
Fe(1)–N(6)	1.960(6)	Fe(1)–N(3)	1.983(3)
Fe(1)–N(1)	1.977(6)	Fe(1)–N(2)	1.983(3)
Fe(1)–N(3)	1.980(6)	Fe(1)–N(5)	2.028(3)

2, and relevant crystallographic data are summarized in Table S1 (Supporting Information). The crystal structures are similar to that of the “parent” complex $[\text{Fe}^{\text{II}}(\text{N4Py})(\text{CH}_3\text{CN})](\text{ClO}_4)_2$ ³¹ and show that the pentadentate ligands L^1 and L^2 coordinate as envisaged, with the sixth coordination site at the iron ion being occupied by a (solvent) acetonitrile molecule. The short Fe–N bond lengths (1.9–2.0 Å) observed for both complexes are in agreement with the presence of low spin Fe(II) centers in $1 \cdot (\text{ClO}_4)_2$ and $2 \cdot (\text{ClO}_4)_2$, as observed for $[\text{Fe}^{\text{II}}(\text{N4Py})(\text{CH}_3\text{CN})](\text{ClO}_4)_2$ ³¹ and some previously reported related Fe(II) complexes.^{24,32,33} A comparison between different Fe–N bond distances in $1 \cdot (\text{ClO}_4)_2$, $2 \cdot (\text{ClO}_4)_2$, and $[\text{Fe}^{\text{II}}(\text{N4Py})(\text{CH}_3\text{CN})](\text{ClO}_4)_2$ is shown in Table 3. It is not possible to discern clear structural trends, as most distances are equivalent within experimental error, but the following observations may be made: For each replacement of a pyridyl moiety by an (*N*-methyl)benzimidazolyl moiety (going from the parent complex to $1 \cdot (\text{ClO}_4)_2$ to $2 \cdot (\text{ClO}_4)_2$), the specific Fe–N bond that is subject to the change is lengthened. Replacement of a pyridyl moiety by a second (*N*-methyl)benzimidazolyl moiety in $2 \cdot (\text{ClO}_4)_2$ results in a lengthening of both equatorial Fe–N_{py} (Py = pyridyl) bond distances with

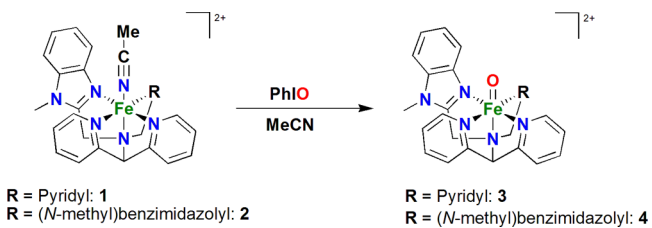
Table 3. Comparison of Different Fe–N Bond Distances (Å) between 1·(ClO₄)₂, 2·(ClO₄)₂, and [Fe^{II}(N4Py)(CH₃CN)](ClO₄)₂³¹

entry	1·(ClO ₄) ₂	2·(ClO ₄) ₂	[Fe ^{II} (N4Py)(CH ₃ CN)](ClO ₄) ₂
Fe–N _{py} (av)	1.953	1.974	1.972
Fe–N _{BzIm} (av)	1.977	1.981	
Fe–N _{MeCN}	1.909(6)	1.901(3)	1.915(3)
Fe–N _{amine}	1.980(6)	2.028(2)	1.961(3)

respect to 1·(ClO₄)₂. This elongation may be rationalized by the angular requirements imposed by the five-membered (*N*-methyl)imidazolyl ring versus the six-membered pyridyl ring, and the consequent structures of the five-membered Fe–N_{amine}–C–C–N_{donor} chelation rings formed upon coordination of the ligands. Thus, the Nδ–C–Nε angles for the benzimidazolyl substituents in 1·(ClO₄)₂ and 2·(ClO₄)₂ vary from 112.2(3)° to 113.2(6)° with the C–C–N_{donor} angles in the corresponding chelate rings varying from 120.1(3)° to 121.0(3)°. For the corresponding pyridyl moiety in 1·(ClO₄)₂, the angles are “reversed”: within the pyridyl ring, C23–C22–N6 = 119.7(11)°, and within the chelation ring, C21–C22–N6 = 114.6(8)°. In other words, the benzimidazolyl units form a more obtuse C–C–N_{donor} angle within the chelation ring than the pyridyl unit, and shortening of the N_{donor}–Fe distance for the benzimidazolyl entities would likely lead to larger strain within the coordination ring. The average Fe–N_{py} bond distance in 1·(ClO₄)₂ is approximately 1.95 Å while the average Fe–N_{py} bond distance in 2·(ClO₄)₂ is approximately 1.97 Å (Table 3). The Fe–N_{amine} bond distance, *trans* to the acetonitrile ligand, is lengthened by approximately 0.05 Å, going from 1·(ClO₄)₂ to 2·(ClO₄)₂.

Generation and Characterization of High Valent Fe(IV) Oxo Complexes. The two Fe(II) complexes contain a relatively labile coordinated solvent (acetonitrile) molecule, and they are easily converted into the corresponding Fe(IV) oxo species upon reaction with the strong O atom donor agent iodosylbenzene (PhIO). Complex 1·(ClO₄)₂ reacted with excess (10 equiv) solid PhIO in acetonitrile at room temperature to form a pale green complex, [Fe^{IV}(O)(L¹)]²⁺ (3) (Scheme 3).

Scheme 3. Generation of the Fe(IV) Oxo Complexes 3 and 4 from the Precursor Fe(II) Complexes 1 and 2, Respectively



Formation of 3 was monitored using UV–vis spectrophotometry, which indicated that complex 1 can be converted into complex 3 within 20 min of stirring at room temperature (Figure S14, Supporting Information). Complex 3 has a characteristic absorbance band in the near IR region, with a maximum at $\lambda_{\text{max}} = 708$ nm and $\epsilon \approx 400$ M⁻¹ cm⁻¹, a common feature for low spin (*S* = 1) Fe(IV) oxo species (Figure 5). Similarly, complex 2·(ClO₄)₂ also formed a pale green species, [Fe^{IV}(O)(L²)]²⁺ (4), upon reaction with excess (10 equiv) PhIO in acetonitrile at low temperature (–10 °C) (Scheme 3).

Complex 4 has a characteristic absorbance band with a maximum at $\lambda_{\text{max}} = 725$ nm with $\epsilon \approx 380$ M⁻¹ cm⁻¹ (Figure 5). These near-IR bands are due to ligand-field (*d*–*d*) transitions centered on the Fe(IV) ion.^{34,35} The change of λ_{max} of the near IR spectral Fe^{IV}=O signature for the complexes [Fe^{IV}(O)(N4Py)]²⁺ (four equatorial pyridyl moieties; $\lambda_{\text{max}} = 695$ nm), 3 (three equatorial pyridyls, one equatorial (*N*-methyl)benzimidazolyl moiety; $\lambda_{\text{max}} = 708$ nm), and 4 (two equatorial pyridyls, two equatorial (*N*-methyl)benzimidazolyl moieties; $\lambda_{\text{max}} = 725$ nm) may be attributed to the change in the ligand environment and suggests that the (equatorial) ligand field becomes progressively weaker as (*N*-methyl)benzimidazolyl substituents are introduced in the ligand scaffold.^{13,18} These absorption maxima may be compared with that of the related, but considerably less stable, complex [Fe^{IV}(O)(ⁿBu-P2DA)] for which $\lambda_{\text{max}} = 770$ nm (ⁿBuP2DA = *N*-(1',1'-bis(2-pyridyl)pentyl)iminodiacetate, *i.e.*, the same ligand framework as L¹, L², and N4Py, but with the two (*N*-methyl)benzimidazolyl moieties of L² replaced by two acetate groups).³⁶ This spectroscopic feature indicates that the ⁿBuP2DA ligand exerts a considerably weaker field than L¹ and L², yet the ground state for [Fe^{IV}(O)(ⁿBu-P2DA)] is *S* = 1. Solomon, Que, and co-workers have deconvoluted the near-IR absorption of [Fe^{IV}(O)(N4Py)]²⁺ using MCD spectroscopy and computational modeling. This relatively broad absorption involves several bands, including a *d*_{xy} to *d*_{xz/yz} transition which is related to the strength of the Fe–O bond and *d*_{xz/yz}–pyridine π overlap, and a *d*_{xy} to *d*_{x²–y²} transition that is directly related to the equatorial field strength of the ligand.^{34b}

Complexes 3 and 4 were also characterized by high resolution mass spectrometry (HRMS). The HRMS of an acetonitrile solution containing complex 3 showed major peaks at *m/z* = 246.0681, corresponding to the formulation [Fe^{IV}(O)(L¹)]²⁺ (*m/z* calcd 246.0675), and at *m/z* = 591.0847, corresponding to the formulation [Fe^{IV}(O)(L¹)(ClO₄)]¹⁺ (*m/z* calcd 591.0841) (Figures S16–18, Supporting Information). Similarly, the HRMS of complex 4 (with triflate counteranion, derived from [Fe^{II}(L²)(CH₃CN)](CF₃SO₃)₂, *cf.*, Experimental Section for synthesis) in acetonitrile showed major peaks at *m/z* = 272.5837, corresponding to the formulation [Fe^{IV}(O)(L²)]²⁺ (*m/z* calcd 272.5808) and at *m/z* = 694.1153, corresponding to the formulation [Fe^{IV}(O)(L²)(CF₃SO₃)]¹⁺ (*m/z* calcd 694.1142) (Figures S19–21, Supporting Information).

Mössbauer spectroscopy was employed to confirm the oxidation state of the iron ions in complexes 3 and 4. The zero-field Mössbauer spectrum of an acetonitrile solution containing a partly (20%) of ⁵⁷Fe enriched sample of 3 showed an isomeric shift value, $\delta = -0.03$ mm s⁻¹, and quadrupole splitting value, $\Delta E_{\text{Q}} = 1.1$ mm s⁻¹ (Figure 6), indicating the presence of an Fe(IV) species. Approximately 86% of the Fe sample accounts for the presence of 3, with the remaining absorption corresponding to an Fe(III) byproduct. In the case of [Fe^{IV}(O)(ⁿBu-P2DA)] (*vide supra*), a corresponding Fe(III) impurity has been suggested to be an (L)Fe^{III}–O–Fe^{III}(L) species,³⁶ and the Mössbauer parameters of the present impurity ($\delta = 0.45$ mm s⁻¹; $\Delta E_{\text{Q}} = 1.50$ mm s⁻¹) are similar to those of the dinuclear ⁿBu-P2DA complex ($\delta = 0.46$ mm s⁻¹; $\Delta E_{\text{Q}} = 1.65$ mm s⁻¹). We therefore tentatively assign the ferric impurity as [({L¹}Fe)₂(μ -O)]⁴⁺, generated by coupling of the analogous Fe^{IV}=O species with its Fe(II) precursor, although, unlike the dinuclear ⁿBu-P2DA complex, the existence of such an Fe(III)–O–Fe(III) dimer could not be confirmed by mass

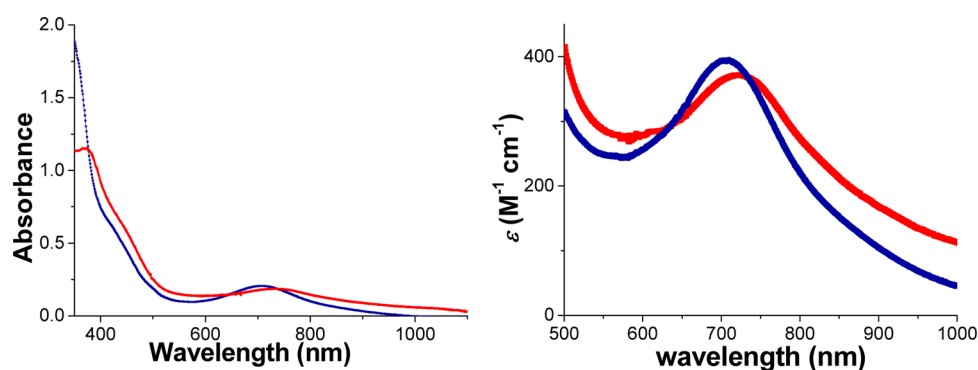


Figure 5. Absorbance spectra of complexes **3** (blue) and **4** (red) [0.5 mM] in acetonitrile (left) recorded at room temperature; expanded plot at long wavelengths, with corresponding molar extinction coefficient values (ϵ) for complexes **3** (blue) and **4** (red) (right).

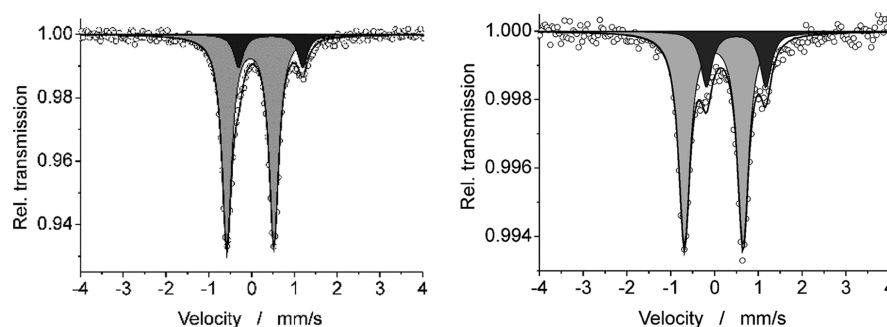


Figure 6. (Left) Zero-field Mössbauer spectrum of ^{57}Fe enriched **3** (light gray) in acetonitrile solution (5 mM) measured at 80 K. The minor black subspectrum corresponds to ca. 14% of an Fe(III) impurity, tentatively assigned as the oxo-bridged dinuclear complex $[\{(\text{L}^1)\text{Fe}\}_2(\mu\text{-O})]^{4+}$ (see text). (Right) Zero-field Mössbauer spectrum of ^{57}Fe enriched **4** (light gray) in acetonitrile solution (2 mM) measured at 80 K. The minor black subspectrum corresponds to ca. 20% of an Fe(III) impurity, tentatively assigned as $[\{(\text{L}^2)\text{Fe}\}_2(\mu\text{-O})]^{4+}$.

spectrometric measurements on **3** (or **4**, *vide infra*). Similarly to **3**, the Mössbauer spectrum of **4** measured under the same conditions showed an isomeric shift value, $\delta = -0.02 \text{ mm s}^{-1}$, and quadrupole splitting value, $\Delta E_{\text{Q}} = 1.34 \text{ mm s}^{-1}$, indicating the presence of an Fe(IV) species, with $\sim 80\%$ of the Fe sample accounting for the presence of **4** (Figure 6). The isomeric shift values for **3** and **4** are very similar to those obtained for $[\text{Fe}^{\text{IV}}(\text{O})(\text{N4Py})]^{2+}$ ($\delta = -0.04 \text{ mm s}^{-1}$; $\Delta E_{\text{Q}} = 0.93 \text{ mm s}^{-1}$)¹³ and $[\text{Fe}^{\text{IV}}(\text{O})(\text{Bn-tpen})]^{2+}$ ($\delta = 0.01 \text{ mm s}^{-1}$; $\Delta E_{\text{Q}} = 0.87 \text{ mm s}^{-1}$),¹³ suggesting that both **3** and **4** are low spin ($S = 1$) nonheme Fe(IV) oxo complexes, and DFT calculations (*vide infra*) support the low spin state as the favored (ground) state. Again, a ferric impurity/byproduct assigned as the oxo-bridged dimer $[\{(\text{L}^2)\text{Fe}\}_2(\mu\text{-O})]^{4+}$ ($\delta = 0.49 \text{ mm s}^{-1}$; $\Delta E_{\text{Q}} = 1.36 \text{ mm s}^{-1}$) was detected (Figure 6).

The half-lives ($t_{1/2}$'s) for complexes **3** and **4** were determined at room temperature. The $t_{1/2}$ for complex **3** is 40 h, while for complex **4** it is 2.5 h, demonstrating that complex **4** is thermally much less stable compared to complex **3**. In Table 4, the half-lives and the characteristic wavelengths of these two new Fe(IV) oxo complexes are compared to some previously reported low spin Fe(IV) oxo complexes bearing pentadentate ligands; it may be noted that the thermal stability of complex **3** is very similar to that of the parent N4Py complex.

Hydrogen-Atom Transfer (HAT) Reactions. The Fe(IV) oxo complexes **3** and **4** react with the C–H bonds of a number of substrates at room temperature. A series of alkane substrates having different C–H bond dissociation energies (BDE) (range from 81 to 99.3 kcal/mol) were investigated, and the relative reactivities between complexes **3** and **4** were evaluated.

Table 4. Comparison of Wavelengths and Half-Lives of Different Low Spin ($S = 1$) Fe(IV) Oxo Complexes Bearing Pentadentate Ligands

complex	λ_{max} nm (ϵ in $\text{M}^{-1} \text{cm}^{-1}$)	$t_{1/2}$ at RT	ref
$[\text{Fe}^{\text{IV}}(\text{O})(\text{L}^1)]^{2+}$ (3)	708 (400)	40 h	this work
$[\text{Fe}^{\text{IV}}(\text{O})(\text{L}^2)]^{2+}$ (4)	725 (380)	2.5 h	this work
$[\text{Fe}^{\text{IV}}(\text{O})(\text{N4Py})]^{2+}$	696 (400)	60 h	13
$[\text{Fe}^{\text{IV}}(\text{O})(\text{t}^{\text{Bu}}\text{-P2DA})]$	770 (220)	n.a.	36
$[\text{Fe}^{\text{IV}}(\text{O})(\text{Bn-tpen})]^{2+}$	739 (400)	6 h	13
$[\text{Fe}^{\text{IV}}(\text{O})(\text{TMC-py})]^{2+}$	834 (260)	7 h	37
$[\text{Fe}^{\text{IV}}(\text{O})(\text{Me}_3\text{cyclam-CH}_2\text{C}(\text{O})\text{NMe}_2)]^{2+}$	810 (270)	5 d	38
$[\text{Fe}^{\text{IV}}(\text{O})(\text{BP}^1)]^{2+}$	730 (400)	n.a.	39
$[\text{Fe}^{\text{IV}}(\text{O})(\text{BP}^2)]^{2+}$	730 (380)	n.a.	39
$[\text{Fe}^{\text{IV}}(\text{O})(\text{MePy}_2\text{TACN})]^{2+}$	736 (310)	n.a.	40
$[\text{Fe}^{\text{IV}}(\text{O})(\text{Me}^2\text{TACNPy}_2)]^{2+}$	740 (340)	n.a.	18

Addition of 20 equiv of triphenylmethane (C–H BDE = 81 kcal/mol) to **3** resulted in rapid decay of **3** to its Fe(II) precursor species as identified by UV–vis spectroscopy (Figure S22, Supporting Information) and formation of triphenylmethanol with $\sim 89\%$ yield. On the other hand, complex **3** reacted with the comparatively less reactive substrate cyclohexane (C–H BDE = 99.3 kcal/mol) at a slower rate to form cyclohexanol (A) and cyclohexanone (K) (yield of A $\sim 8\%$, yield of K $\sim 10\%$, total yield $\sim 18\%$). Similarly, complex **4** reacted with triphenylmethane with a faster rate producing triphenylmethanol with $\sim 90\%$ yield (Figure 7, left), while its reactivity slowed for

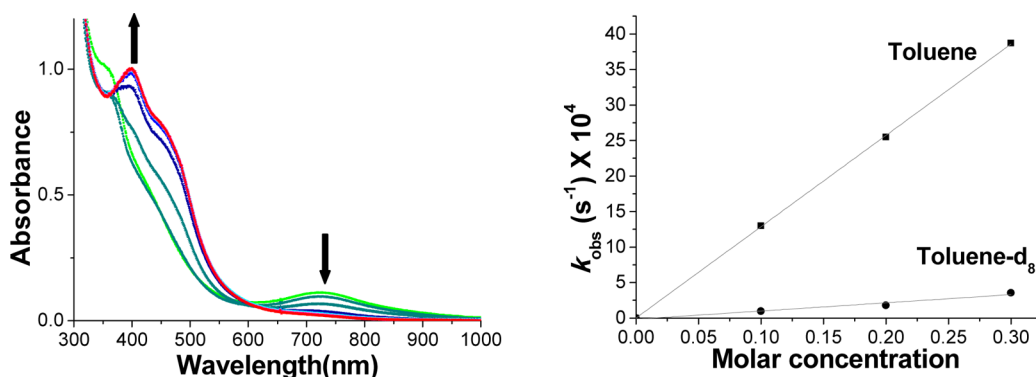


Figure 7. (Left) Kinetic decay of complex 4 (≈ 0.5 mM in acetonitrile) upon addition of 30 equiv of triphenylmethane at room temperature. The decay product is most likely a mixture of complex 2 and the byproduct $[\{(L^2)Fe\}_2(\mu-O)]^{4+}$, meaning that the 477 nm band of 2 grows in as a shoulder in the spectrum. (Right) Determination of the kinetic isotope effect (KIE) for separate reactions with toluene and toluene- d_8 with complex 3 at room temperature.

Table 5. C–H Bond Dissociation Energies of Different Alkane Substrates and the Second-Order Rate Constants (k_2) of 3, 4, and $[Fe^{IV}(O)(N4Py)]^{2+}$ for HAT Reactivities

substrate	BDE (kcal/mol)	$k_2 \times 10^3$ for 3 ($M^{-1} s^{-1}$)	$k_2 \times 10^3$ for 4 ($M^{-1} s^{-1}$)	$k_2 \times 10^3$ for $[Fe^{IV}(O)(N4Py)]^{2+}$ ($M^{-1} s^{-1}$) ¹⁴
triphenylmethane	81	31 ± 1	270 ± 10	37.0
cumene	84.5	8 ± 0.3	60 ± 1	2.0
ethylbenzene	87	7.6 ± 0.2	48 ± 1	4.0
toluene	90	1.3 ± 0.4	12 ± 5	0.15
cyclooctane	95.3	1.5 ± 0.1	26 ± 1	
2,3-dimethyl butane	96.5	0.32 ± 0.03	2.5 ± 0.3	0.12
cyclohexane	99.3	0.3 ± 0.02	2.9 ± 0.1	0.05

^aAdapted from ref 14.

substrates with higher C–H BDE. The details of product analyses are provided in the [Supporting Information](#). The decay of the Fe–oxo absorbance band of 3 monitored at 708 nm (and of 4 monitored at 725 nm) followed pseudo-first-order conditions in the presence of excess substrate (50–400 equiv) for a range of substrates. The second-order rate constants (k_2) for the different substrates were obtained from the slope of plots of the observed pseudo-first-order rate constant, k_{obs} , versus molar concentration, taken at three different substrate concentrations. The k_2 values thus obtained are listed in [Table 5](#).

A plot of logarithmic values of second-order rate constants ($\log k_2'$) (k_2' is the second-order rate constant divided by the number of equivalent C–H bonds in the substrate) for absorbance decay versus bond dissociation energies for various hydrocarbons shows a linear correlation ([Figure 8](#)).

A primary kinetic isotope effect (KIE) value of ~ 14 was obtained by determining the second-order rate constants corresponding to separate reactions of toluene and its d_8 -isotopomer with 3 ([Figure 7](#), right), using the same methodology as that described above. The corresponding KIE value for 4 was ~ 11 . The linear correlation between $\log k_2'$ and C–H BDE of substrates, as well as the observed large KIE value, constitutes strong evidence of the reactions taking place via hydrogen-atom transfer (HAT). The above-mentioned KIE values are larger than “classical” KIE values (which are expected to be less than or equal to 7) but lower than that observed for the reaction of $[Fe^{IV}(O)(N4Py)]^{2+}$ (KIE ~ 20).⁴¹ Klinker et al. have argued that the relatively high KIE value for $[Fe^{IV}(O)(N4Py)]^{2+}$ may be explained by a tunneling-like HAT mechanism involving a crossover from a triplet ($S = 1$) ground state to a quintet ($S = 2$) transition state (two-state reactivity,

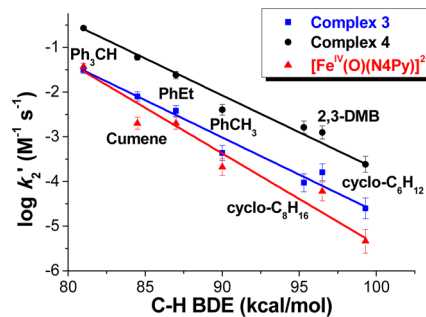


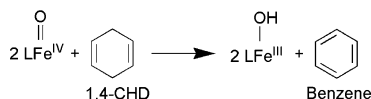
Figure 8. Plot of $\log k_2'$ versus C–H bond dissociation energies of different alkane substrates for 3 and 4 and $[Fe^{IV}(O)(N4Py)]^{2+}$ (adapted from ref 14) with 5% error range. The second-order rates were measured at 25 °C in all cases.

TSR, *vide infra*).⁴¹ The nonclassical values observed for 3 and 4 suggest that these complexes follow similar reaction paths as $[Fe^{IV}(O)(N4Py)]^{2+}$ (*cf.*, [Discussion](#)).

The reactivity of complex 4 with substrates like 9,10-dihydroanthracene (9,10-DHA) and 1,4-cyclohexadiene (1,4-CHD) was also investigated in order to examine any possible influence of the bulky (*N*-methyl)benzimidazolyl moieties on the access to the Fe(IV) oxo center by the substrate. Both substrates have similar C–H bond dissociation energies (C–H BDE = 77 kcal/mol for 9,10-DHA and 78 kcal/mol for 1,4-CHD), but 9,10-DHA is a sterically bulkier substrate relative to 1,4-CHD. The second-order rate constants obtained for complex 4 measured at 243 K were $(1.4 \pm 0.2) M^{-1} s^{-1}$ with 9,10-DHA and $(1.2 \pm 0.3) M^{-1} s^{-1}$ with 1,4-CHD. Similar values of k_2 for 4 indicated that access to the Fe(IV) oxo center by the substrates were equally feasible and not influenced by

the nearby (*N*-methyl)benzimidazolyl arms. It should be mentioned that **4** acted as a one-electron oxidant in these cases, thereby requiring 2 equiv of complex **4** to form benzene (identified by GC) from 1 equiv of 1,4-CHD (Scheme 4).

Scheme 4. Reaction of an Fe(IV) Oxo Complex with 1,4-Cyclohexadiene



While the steric hindrance in complex **4** has not been probed by an extensive range of substrates, the results above indicate that there is relatively little steric discrimination of substrates by **4** (and implicitly by **3**).

The HAT plot clearly indicates that **4** consistently reacted with faster rates of reactions with different hydrocarbon substrates with respect to **3**. The slopes observed for the HAT plots of $[\text{Fe}^{\text{IV}}(\text{O})(\text{N4Py})]^{2+}$,¹³ complex **3**, and complex **4** are not parallel (Figure 8), but the approximate colinearity of the plots/slopes for the different complexes indicates that the effect in reaction rates upon introducing the second (*N*-methyl)benzimidazolyl arm is roughly the same irrespective of the substrate. Considering that there does not seem to be a significant steric discrimination of substrates for complex **4** (*vide supra*), the observed HAT reactivities suggest that the influence of the replacement of a pyridyl side arm by a (*N*-methyl)benzimidazolyl side arm is primarily electronic. Since the reaction of an Fe(IV) oxo species with a substrate R–H involves the rate-determining transfer of a hydrogen-atom (one electron coupled with a proton), it may be concluded that the effective hydrogen-atom affinity of the ferryl unit is increased by the successive introduction of (*N*-methyl)benzimidazolyl side arms in this family of complexes; it may be noted that the addition of one extra (*N*-methyl)benzimidazolyl moiety increases the rate constant by 1 order of magnitude (Figure 8).

O-Atom Transfer (OAT) Reactions: Oxidation of Sulfides. The oxo transfer reactivities of **3** and **4** were also investigated, using thioanisole (PhSCH₃) as a substrate. Complex **3** reacted with thioanisole at 243 K and transferred the oxygen to form methyl phenyl sulfoxide in high yield (~84%) (Scheme 5). During the course of the reaction, complex **3** was converted into its Fe(II) precursor (complex **1**) as identified by UV–vis spectrophotometry (Figure 9). The reaction showed pseudo-first-order behavior under conditions of excess of substrate (5–20 equiv with regard to complex **3**), and the observed rate constant (k_{obs}) was linearly dependent on substrate concentration (Figure 9). From this linear plotting, a second-order rate constant (k_2) with a value of $(3.3 \pm 0.09) \times$

$10^{-2} \text{ M}^{-1} \text{ s}^{-1}$ was obtained in the oxidation of thioanisole by complex **3**. Similarly, **4** was reacted with thioanisole under the same conditions, and a faster rate with respect to complex **3** and methyl phenyl sulfoxide was obtained with a yield of ~88%. The second-order rate constant (k_2) for complex **4** in oxo transfer reaction was found to be $(3.1 \pm 0.11) \times 10^{-1} \text{ M}^{-1} \text{ s}^{-1}$. Table 6 shows a comparison in the reaction rates of OAT processes between complex **3**, **4**, and previously reported Fe(IV) oxo complexes. In parallel with the observed trend for HAT, the k_2 values suggest that complex **4** is more reactive (by 1 order of magnitude) than complex **3** in the OAT reaction (*i.e.*, thioanisole oxidation).

DISCUSSION

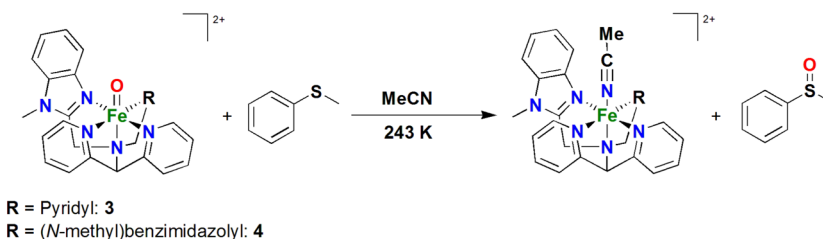
The enhanced HAT and OAT reactivities of **3** and **4** when compared with $[\text{Fe}^{\text{IV}}(\text{O})(\text{N4Py})]^{2+}$ may be considered using two popular approaches:^{33,42} Shaik's exchange-enhanced-reactivity (EER) model¹⁵ and/or the Bell–Evans–Polanyi principle (BEP) of linear free energy relations (LFER),^{43,44} which has been fruitfully developed by Mayer for HAT reactions.⁴⁵ These approaches are not mutually exclusive but rather complementary, as the EER approach applies to the kinetics and the BEP to the thermodynamics of the process.

According to the EER, or two-state reactivity (TSR) model,^{14b,46} the HAT reactivity of triplet $\text{Fe}^{\text{IV}}=\text{O}$ ($S = 1$) complexes may be explained by a more reactive quintet ($S = 2$) transition state that is populated via spin crossover during movement over the energy surface along the reaction coordinate. The EER/TSR model shows that an increase of the number of unpaired and spin-identical electrons on the iron center will be favorable to the reactivity of the high spin state in comparison with that of the low spin state. The model states that a greater number of unpaired electrons will lead to a more favorable transition state (hence increased reactivity), and therefore, the proximity of the quintet excited state to the triplet ($S = 1$) ground state in the $\text{Fe}^{\text{IV}}=\text{O}$ complex and correspondingly the easiness of triplet/quintet spin crossover is significant for its reactivity. Oxygen-atom transfer reactions are two-electron processes and hence should not exhibit EER.⁴⁶ The TSR model is difficult to verify experimentally, and the concept that a high spin (transition) state is inherently more reactive than a low spin (transition) state has been challenged. Computational modeling by Que, Solomon, and co-workers has shown that the reaction barriers for HAT involving $[\text{Fe}^{\text{IV}}(\text{O})-(\text{TMG}_3\text{tren})]^{2+}$ ($S = 2$) and $[\text{Fe}^{\text{IV}}(\text{O})(\text{N4Py})]^{2+}$ ($S = 1$) are composed of electronic components that are approximately similar, while the difference in reactivity of the two complexes is due to different steric contributions to the reaction barrier.⁴⁷

In order to elucidate the HAT mechanism(s) for reaction of alkanes with **3** and **4**, and establish the spin states of the active

Scheme 5. Oxygen-Atom Transfer (OAT) to Thioanisole by Complex 3 and 4 at 243 K

O-atom transfer (OAT) reactions: Oxidation of sulfides



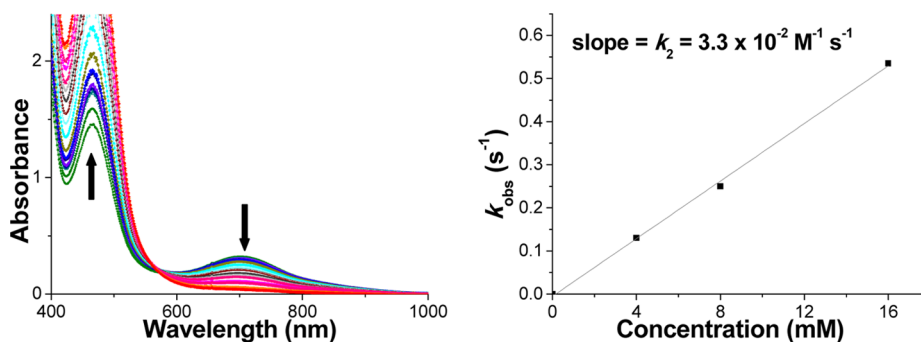


Figure 9. (Left) Conversion of complex 3 into its Fe(II) precursor in the presence of thioanisole (5 equiv) at 243 K. (Right) Determination of the second-order rate constant for the oxygen-atom transfer reaction from the k_{obs} vs concentration plot.

Table 6. Comparison of Rates of OAT Process (Thioanisole Oxidation) between Complex 3, Complex 4, and Some Other Relevant Low Spin Fe(IV) Oxo Complexes

complex	k_2 (in $\text{M}^{-1} \text{s}^{-1}$)	temp of measurement	ref
$[\text{Fe}^{\text{IV}}(\text{O})(\text{L}^1)]^{2+}$ (3)	3.3×10^{-2}	243 K	this work
$[\text{Fe}^{\text{IV}}(\text{O})(\text{L}^2)]^{2+}$ (4)	3.1×10^{-1}	243 K	this work
$[\text{Fe}^{\text{IV}}(\text{O})(\text{N4Py})]^{2+}$	1.4×10^{-2}	263 K	18
$[\text{Fe}^{\text{IV}}(\text{O})(\text{N4Py})]^{2+}$	2.4×10^{-4}	233 K	15
$[\text{Fe}^{\text{IV}}(\text{O})(\text{Bn-tpen})]^{2+}$	3.3×10^{-1}	263 K	18
$[\text{Fe}^{\text{IV}}(\text{O})(\text{Bn-tpen})]^{2+}$	1.4×10^{-2}	233 K	15
$[\text{Fe}^{\text{IV}}(\text{O})(\text{Me}_3\text{NTB})]^{2+}$	2.1×10^4	233 K	15

species on the potential energy surface, DFT calculations were carried out on the triplet and quintet states of 3 (^3A and ^5A), using methane (B) as the substrate. Figure 10 shows the lowest

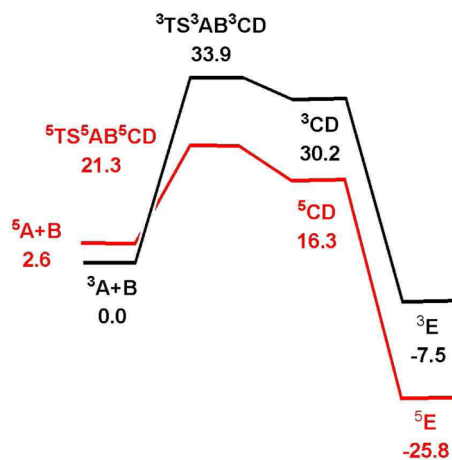


Figure 10. B3LYP potential energy surface for reaction of $^3\text{A}/^5\text{A}$ and methane (B) to give methanol-substituted complexes ^3E and ^5E . Energy values are in ΔG in kcal/mol relative to $^3\text{A} + \text{B}$.

energy pathways that have been computed for methane activation, while Figure 11 shows the pertinent transition-state structures responsible for H-abstraction. The results are in concert with a two-state reactivity model, as popularized by Shaik, involving the triplet ($S = 1$) and quintet ($S = 2$) reaction surfaces.^{14b,48–50}

The side-on approach of methane to the oxo moiety in ^3A leads to $^3\text{TS}^3\text{AB}^3\text{CD}$ through a π -directed manifold. This transition structure lies 33.9 kcal/mol above the triplet oxo ^3A and affords the corresponding geminate radical pair

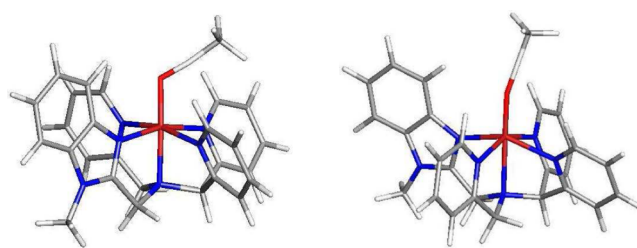


Figure 11. B3LYP-optimized transition-state structures $^3\text{TS}^3\text{AB}^3\text{CD}$ (left) and $^5\text{TS}^5\text{AB}^5\text{CD}$ (right).

$[\text{Fe}^{\text{III}}(\text{OH})(\text{L}^1)]^{2+}$ (C) and methyl radical D. Collapse of ^3CD completes the formal hydroxylation and gives the MeOH-coordinated complex $[\text{Fe}^{\text{II}}(\text{MeOH})(\text{L}^1)]^{2+}$ (^3E). The overall process is exergonic by 7.5 kcal/mol.

Population of the energetically favored quintet surface proceeds through a $^3\text{A} \rightarrow ^5\text{A}$ spin crossover. The quintet oxo species (^5A) undergoes HAT reaction through a linear, σ -directed transition structure, $^5\text{TS}^5\text{AB}^5\text{CD}$, which lies 12.6 kcal/mol lower in energy than the triplet transition structure ($^3\text{TS}^3\text{AB}^3\text{CD}$). This energetic stabilization more than compensates for the ground-state exchange destabilization experienced by ^5A . The collapse of the geminate radical pair, ^5CD , affords the MeOH-coordinated complex $[\text{Fe}^{\text{II}}(\text{MeOH})(\text{L}^1)]^{2+}$ (^5E) with a net release of 25.8 kcal/mol.⁵¹

The experimental observation of an increase in the rate of HAT for each successive substitution of a pyridyl unit in $[\text{Fe}^{\text{IV}}(\text{O})(\text{N4Py})]^{2+}$ by (*N*-methyl)benzimidazolyl moiety is also supported by DFT calculations. The calculated barrier for HAT of methane by 3 is 1.9 kcal/mol lower in energy than that for $[\text{Fe}^{\text{IV}}(\text{O})(\text{N4Py})]^{2+}$ ($\Delta G^\ddagger = 23.2$ kcal/mol). The same barrier calculated for 4 ($\Delta G^\ddagger = 20.5$ kcal/mol) is an additional 0.8 kcal/mol lower in energy. We are convinced that the computed trend is correct, but it should be noted that these differences in activation energies, which are based on gas phase calculations, may not be expected to be quantitatively translated to observed reaction rates.

The BEP/LFER principle establishes the linear correlation of the reaction barrier height ($\Delta\Delta G^\ddagger$) with the thermodynamic driving force of reaction determined by the free energy value ($\Delta\Delta G^\circ$). Such linear free energy relationships have been established for a wide range of heme and nonheme ferryl complexes.⁵² According to Mayer,⁴⁵ the reactivities of $\text{Fe}^{\text{IV}}=\text{O}$ complexes in HAT reactions may be related to their redox potentials and the $\text{p}K_a$ of the $\text{Fe}-\text{OH}$ products according to the Bordwell–Polanyi equation.

$$D_{\text{OH}} = 23.06E^\circ + 1.37pK_a + C$$

The rates of HAT reactions effected by ferryl species should thus be mainly correlated to the redox potentials of $\text{Fe}^{\text{IV}}=\text{O}$ complexes, with potential deviations related to contributions by the second term of this equation (pK_a) or the nonadiabaticity of the reaction (EER model). For equatorial donors an increase of the donor strength of the ligand will lower the redox potential of the $\text{Fe}^{\text{IV}}=\text{O}$ moiety and increase the pK_a of the $\text{Fe}^{\text{III}}-\text{OH}$ product formed upon hydrogen-atom transfer. It has been found that ligand donor moieties in *cis*-position to the oxo unit (equatorial donors) exert less influence on the reactivity of $\text{Fe}^{\text{IV}}=\text{O}$ ($S = 1$) octahedral complexes as compared to those ligated *trans* (axial)⁴⁸ as “*trans*-ligands can interact with both σ - and π -orbitals involved in the $\text{Fe}=\text{O}$ bond but *cis*-ligands cannot”.⁵³ However, in the present case, the effect of replacing equatorial pyridyl donors with (*N*-methyl)benzimidazolyl units is quite significant. The (number and positions of) equatorial donors in octahedral complexes can modulate the spin state and reactivity of the oxo unit by altering the energies, and thus the occupancies, of the iron d_{xy} and $d_{x^2-y^2}$ orbitals. The relative λ_{max} of the low energy d–d bands in the series $[\text{Fe}^{\text{IV}}(\text{O})(\text{N4Py})]^{2+}$, **3**, and **4** indicate that the replacement of equatorial pyridyl moieties by (*N*-methyl)benzimidazolyl units leads to a weaker ligand field but is still sufficiently strong to support a $d_{xy}/d_{x^2-y^2}$ gap in the $\text{Fe}^{\text{IV}}=\text{O}$ complexes that leads to spin pairing to form the $S = 1$ ground states for **3** and **4**. Still, the weaker ligand field provided by the (*N*-methyl)benzimidazolyl units should decrease the triplet/quintet gap relative to that of $[\text{Fe}^{\text{IV}}(\text{O})(\text{N4Py})]^{2+}$. This is in fact what our DFT calculations show with $\Delta G_{\text{TQ}} = 4.0$ kcal/mol for $[\text{Fe}^{\text{IV}}(\text{O})(\text{N4Py})]^{2+}$, $\Delta G_{\text{TQ}} = 2.6$ kcal/mol for **3**, and $\Delta G_{\text{TQ}} = 1.7$ kcal/mol for **4**. The decrease of field strength may thus, in principle, facilitate the spin crossover required for two-state reactivity (*vide supra*) and can thus explain the increase in HAT rates that are observed upon substitution of pyridyl moieties by (*N*-methyl)benzimidazolyl moieties in the ligand framework.

It has previously been found that the activities of $\text{Fe}^{\text{IV}}=\text{O}$ complexes with tetramethylcyclam (TMC) ligands in oxygen-atom transfer reactions correlate directly with the electrophilicity of the $\text{Fe}^{\text{IV}}=\text{O}$ moiety.¹² One may thus expect complexes **3** and **4** to be less electrophilic and poorer OAT reagents than $[\text{Fe}^{\text{IV}}(\text{O})(\text{N4Py})]^{2+}$; however, our results show that the trend is the opposite. The redox properties of **3** and **4** will need to be established in order to establish a quantitative correlation to the OAT reactivities of the $\text{Fe}^{\text{IV}}=\text{O}$ complexes.

SUMMARY AND CONCLUSIONS

The octahedral ferryl complexes **3** ($t_{1/2} = 40$ h, RT) and **4** ($t_{1/2} = 2.5$ h, RT) with pentadentate N_5 -donor ligands (*cf.*, Table 5) that have been prepared by us are significantly more stable than the previously studied $[\text{Fe}^{\text{IV}}(\text{O})(\text{Me}_3\text{NTB})]^{2+}$ complex, and have thus permitted a detailed study of ferryl complexes with (*N*-methyl)benzimidazolyl donor moieties. More importantly, **3** and **4** demonstrated excellent hydrogen-atom transfer (HAT) and oxygen-atom transfer (OAT) activities, surpassing the parent $[\text{Fe}^{\text{IV}}(\text{O})(\text{N4Py})]^{2+}$ complex by approximately 1–2 orders of magnitude (Tables 5 and 6, Figure 8). For example, in the oxidation of cyclohexane (which has the strongest C–H bonds among the substrates used in the present study) the successive replacement of pyridyl moieties of the N4Py ligand by one and two (*N*-methyl)benzimidazolyl moieties led to

increases in the corresponding values for the rate constants by 1 order of magnitude for each nitrogen donor replacement. Despite the increased steric bulk of the (*N*-methyl)benzimidazolyl groups relative to the pyridyl moieties, no influence of this replacement on the access to the $\text{Fe}(\text{IV})$ oxo center by the substrate molecules could be detected.

As expected, the introduction of equatorial (*N*-methyl)benzimidazolyl donors in the N4Py framework reduces the energy difference between the iron d_{xy} and $d_{x^2-y^2}$ orbitals, but the resulting $d_{xy}/d_{x^2-y^2}$ gap is not sufficiently small to make the high spin $S = 2$ state the ground state of **3** and **4**. However, even though DFT calculations find the low spin $S = 1$ state to be the ground state for both **3** and **4**, computational modeling of the HAT/hydroxylation of methane by **3** and **4** (*vide supra*) supports spin crossover, since the high spin $S = 2$ transition states for **3** and **4** are preferred over the low spin $S = 1$ transition state by, respectively, 12.6 and 15.1 kcal/mol.

EXPERIMENTAL SECTION

Materials. The reagents and solvents were purchased from Sigma-Aldrich and Fisher chemicals. All solvents were of at least 99.5% purity and used as received. Reagents were of at least 99% purity and used without any further purification. *N*-[Di(2-pyridinyl)methyl]-*N*-(2-pyridinylmethyl)methylamine,²⁹ bis(2-pyridyl)methylamine,³⁰ and 2-chloromethyl-1-methylbenzimidazole⁵⁴ were prepared according to literature procedures.

Physical Methods. UV–vis spectra and all kinetic experiments were performed on a 8453 UV–vis Agilent Technologies equipped with a diode-array detector and a Unisoku which permits monitoring of the temperature of the experiments from -90 to 100 °C. All UV–vis spectra were measured in 1 cm quartz cell. NMR spectra were collected on Varian Inova 500 MHz spectrometer in CDCl_3 and CD_3CN solvents and referenced to the residual signal of the solvent. Elemental analysis was performed using an ElementarVario EL III instrument. The mass spectrometry (ESI) was performed with a Bruker HCT ultra mass spectrometer. The high resolution mass spectrum (HRMS) was performed using a Bruker FTICR APEX IV instrument. The electrochemical analyses were performed on a model CHI760B Electrochemical Workstation (CH Instrument). Tetrabutylammonium hexafluorophosphate $[(t\text{-Bu}_4\text{N})\text{HPF}_6]$ was used as a supporting electrolyte, and the measurements were carried out using 3 mm diameter Teflon-shrouded glassy carbon working electrode, a Pt wire auxiliary electrode, and an SCE reference electrode. Product analyses were performed on an Agilent technologies 7820A with 16 sample automatic liquid sampler and flame ionization detector. The products were identified by their GC retention times. Mössbauer spectra were recorded with a ⁵⁷Co source in a Rh matrix using an alternating constant acceleration Wissel Mössbauer spectrometer operated in the transmission mode and equipped with a Janis closed-cycle helium cryostat. Isomer shifts are given relative to iron metal at ambient temperature. Simulation of the experimental data was performed with the *Mfit* program (E. Bill, Max-Planck Institute for Chemical Energy Conversion, Mülheim/Ruhr, Germany).

Synthesis of Ligand L¹ [N-(1-Methyl-2-benzimidazolyl)methyl-N-(2-pyridyl)methyl-N-(bis-2-pyridylmethyl)amine]. A two-necked round-bottom flask was charged with *N*-[di(2-pyridinyl)methyl]-*N*-(2-pyridinylmethyl)methylamine (1.00 g, 3.6 mmol), 2-chloromethyl-1-methylbenzimidazole (0.651 g, 3.6 mmol), K_2CO_3 (2.5 g, 18 mmol), and tetrabutylammonium bromide (0.23 g, 0.7 mmol). A total of 50 mL of dry CH_3CN was added under a vigorous flow of nitrogen. The mixture was refluxed for 24 h under nitrogen, and then the reaction mixture was filtered through a Celite pad. A small amount of CH_2Cl_2 was added to wash the Celite pad. The resulting filtrate was evaporated, and the residue was dissolved in a 1 (M) NaOH solution and extracted with CH_2Cl_2 . The organic portion was washed with brine solution and dried over Na_2SO_4 . Evaporation of the organic solvent gave the crude ligand L¹ as a red oil. This crude product was purified by passing through a silica column using a mixture of

$\text{CH}_2\text{Cl}_2:\text{CH}_3\text{OH}:\text{Et}_3\text{N}$ (10:2:1) as eluent. Yield: 1.01 g (67%). ESI-MS: 421.2 $[\text{M} + \text{H}]^+$. ^1H NMR (500 MHz, CDCl_3) δ (ppm): 8.6–8.55 [m, 3H, Py-H], 7.76 [d, 2H, $J = 8$ Hz, BzIm-H], 7.69–7.6 [m, 3H, Py-H], 7.5 [m, 3H, Py-H], 7.2–7.15 [m, 5H, BzIm-H, Py-H], 5.33 [s, 1H, NCH], 4.18 [s, 2H, NCH_2Py], 3.98 [s, 2H, NCH_2BzIm], 3.75 [s, 3H, NCH_3]. ^{13}C NMR (125 MHz, CDCl_3) δ (ppm): 159.58 (s), 159.21 (s), 152.0 (s), 149.38 (s), 148.98 (s), 136.52 (s), 136.1 (s), 124.65 (s), 123.72 (s), 122.39 (d), 121.885 (d), 119.580 (s), 72.14 (s), 57.63 (s), 49.36 (s), 30.25 (s).

Synthesis of Ligand L^2 [*N*-Bis(1-methyl-2-benzimidazolyl)methyl-*N*-(bis-2-pyridylmethyl)amine]. A total of 0.403 g of 2-chloromethyl-1-methylbenzimidazole (2.23 mmol) was dissolved in 2 mL of a 5 M NaOH solution. After about 10 min of stirring, bis(2-pyridyl)methylamine (0.206 g, 1.115 mmol) in 2 mL of 5 M NaOH was added. The stirring was continued for 3 days at room temperature. After stirring was finished, the sticky solid that was formed was collected, and HPF_6 was added dropwise to precipitate a brick-red solid. The resultant solid was dissolved in hot water. After recrystallization from hot water, 5 M NaOH was added to basify the reaction mixture ($\text{pH} > 12$). The product was extracted with dichloromethane and dried over Na_2SO_4 , and the dichloromethane extract was evaporated to give the desired ligand L^2 as a pale brownish solid. Yield: 0.749 g (71%). ESI-MS: 474.2 $[\text{M} + \text{H}]^+$. ^1H NMR (500 MHz, CDCl_3) δ (ppm): 8.635 [d, 2H, $J = 8$ Hz, Py-H], 7.714–7.645 [m, 6H, Py-H], 7.62 [dt, 2H, BzIm-H], 7.19 [m, 4H, BzIm-H, Py-H], 5.402 [s, 1H, NCH], 4.285 [s, 4H, NCH_2BzIm], 3.619 [s, 6H, NCH_3]. ^{13}C NMR (125 MHz, CDCl_3) δ (ppm): 158.8 (s), 151.9 (s), 149.15 (s), 136.47 (s), 136.05 (s), 124.97 (s), 122.8 (s), 122.39 (d), 119.41 (s), 109.1 (s), 48.31 (s), 29.8 (s).

Synthesis of $[\text{Fe}^{\text{II}}(\text{CH}_3\text{CN})(\text{L}^1)(\text{ClO}_4)_2(1\text{-}(\text{ClO}_4)_2)]$. A total of 100 mg (0.23 mmol) of ligand L^1 was taken in a vial and dissolved in a minimum amount of CH_3CN . To this solution was added 58.6 mg (0.23 mmol) of $\text{Fe}(\text{ClO}_4)_2$ in CH_3CN under stirring at room temperature under air. A red precipitate appeared within 5 min of stirring. After stirring for about 30 min, the reaction mixture was placed into an ethyl acetate bath and stored overnight. The precipitate was collected by filtration, washed with ethyl acetate, dried under vacuum, and obtained as a red solid. Yield: 147 mg (82%). ESI-MS (in CH_3CN): m/z 238 $[\text{Fe}^{\text{II}}(\text{L}^1)]^{2+}$ ($z = 2$) calcd 238, 258.5 $[\text{Fe}^{\text{II}}(\text{L}^1)(\text{CH}_3\text{CN})]^{2+}$ ($z = 2$) calcd 258.5, 575.1 $[\text{Fe}^{\text{II}}(\text{L}^1)(\text{ClO}_4)]^+$ ($z = 1$) calcd 575.1, 616.1 $[\text{Fe}^{\text{II}}(\text{L}^1)(\text{CH}_3\text{CN})(\text{ClO}_4)]^+$ ($z = 1$) calcd 616.1. Anal. Calcd (%): C 47.58, H 3.99, N 14.8. Found (%): C 46.97, H 3.98, N 14.93. ^1H NMR (500 MHz, CD_3CN , 298 K) δ (ppm): 9.42 [s, 1H, Py-H], 9.165 [d, 2H, $J = 25$ Hz, Py-H], 8.015 [d, 1H, $J = 5$ Hz, BzIm-H], 7.94–7.88 [m, 2H, BzIm-H], 7.61 [t, 1H, $J = 15$ Hz, Py-H], 7.53–7.38 [m, 6H, Py-H], 7.27 [d, 1H, $J = 10$ Hz, BzIm-H], 6.77 [s, 1H, NCH], 4.795 [d, 2H, $J = 15$ Hz, NCH_2Py], 4.57 [dd, 2H, $J = 27.5$, 7.5 Hz, NCH_2BzIm], 3.61 [s, 3H, NCH_3].

Synthesis of $[\text{Fe}^{\text{II}}(\text{CH}_3\text{CN})(\text{L}^2)(\text{ClO}_4)_2(2\text{-}(\text{ClO}_4)_2)]$. The procedure for the synthesis of complex 2 is identical to that for 1. A total of 109 mg (0.23 mmol) of ligand L^2 was taken in a vial and dissolved in a minimum amount of acetonitrile. To this solution, 58.6 mg (0.23 mmol) of $\text{Fe}(\text{ClO}_4)_2$ in acetonitrile was added under stirring at room temperature under air. A red precipitate appeared within 5 min of stirring. After about 30 min of stirring, the reaction mixture was placed into an ethyl acetate bath and stored overnight. The precipitate was collected by filtration, washed with ethyl acetate, dried under vacuum, and obtained as red solid. Yield: 136 mg (77%). ESI-MS (in CH_3CN): m/z 264.6 $[\text{Fe}^{\text{II}}(\text{L}^2)]^{2+}$ ($z = 2$) calcd 264.6, 628.1 $[\text{Fe}^{\text{II}}(\text{L}^2)(\text{ClO}_4)]^+$ ($z = 1$) calcd 628.1. Anal. Calcd (%): C 49.14, H 4.18, N 16.01. Found (%): C 48.99, H 4.17, N 16.77. ^1H NMR (500 MHz, CD_3CN , 298 K) δ (ppm): 18.7 [br, 2H, Py-H], 16.74 [br, 1H, NCH], 12.47 [s, 4H, NCH_2BzIm], 8.48 [s, 6H, NCH_3], 5.62 [s, 2H, Py-H], 5.02 [s, 2H, Py-H], 3.6 [br, 2H, BzIm-H], 3.3 [s, 2H, BzIm].

Synthesis of $[\text{Fe}^{\text{II}}(\text{CH}_3\text{CN})(\text{L}^2)(\text{CF}_3\text{SO}_3)_2(2\text{-}(\text{CF}_3\text{SO}_3)_2)]$. A total of 71 mg (0.15 mmol) of ligand L^2 was taken in a vial and dissolved in a minimum amount of acetonitrile. To this solution, 65.4 mg (0.15 mmol) of $[\text{Fe}(\text{CH}_3\text{CN})_2(\text{CF}_3\text{SO}_3)_2]$ in acetonitrile was added under stirring at room temperature under nitrogen atmosphere. After about 30 min of stirring, the reaction mixture was placed into an ethyl acetate

bath and stored overnight. The precipitate was collected by filtration, washed with ethyl acetate, dried under vacuum, and obtained as red solid. Yield: 101 mg (78%). ESI-MS (in CH_3CN): m/z 264.6 $[\text{Fe}^{\text{II}}(\text{L}^2)]^{2+}$ ($z = 2$) calcd 264.6, 678.1 $[\text{Fe}^{\text{II}}(\text{L}^2)(\text{CF}_3\text{SO}_3)]^+$ ($z = 1$) calcd 678.1. Anal. Calcd (%): C 45.63, H 3.48, N 12.9. Found (%): C 46.05, H 3.27, N 12.53. ^1H NMR (500 MHz, CD_3CN , 298 K) δ (ppm): 18.55, 16.80, 12.40, 8.44, 5.62, 5.04, 3.65, 3.34.

Crystal Structure Determinations. The crystal of 1·(ClO_4)₂ and 2·(ClO_4)₂ were immersed in cryo-oil, mounted in a Nylon loop, and measured at a temperature of 100 K. The X-ray diffraction data were collected on a Bruker Kappa Apex II and Bruker Kappa Apex II Duo diffractometers using Mo $K\alpha$ radiation ($\lambda = 0.71073 \text{ \AA}$). The APEX2⁵⁵ program package was used for cell refinements and data reductions. The structure was solved by charge flipping technique (SUPERFLIP)⁵⁶ or direct methods using the SIR2011⁵⁷ program with the Olex2⁵⁸ graphical user interface. A semiempirical numerical absorption correction based on equivalent reflections (SADABS)⁵⁹ was applied to all data. Structural refinements were carried out using SHELXL-97.⁶⁰ The crystal of 1·(ClO_4)₂ was diffracting only weakly, and therefore, atoms N2, C16, C17, C18, C19, and C20 were restrained to have the same U_{ij} components within the standard uncertainty of 0.02. In 2·(ClO_4)₂ one molecule of the acetonitrile of crystallization was disordered over two sites with equal occupancies. Hydrogen atoms were positioned geometrically and were also constrained to ride on their parent atoms, with $\text{C-H} = 0.95\text{--}0.100 \text{ \AA}$, and $U_{\text{iso}} = 1.2\text{--}1.5U_{\text{eq}}$ (parent atom). The crystallographic details are summarized in Table S1, Supporting Information.

Hydrogen-Atom Transfer (HAT) Reactions. $\text{Fe}(\text{IV})$ oxo solutions (in the concentration range 0.5–1.0 mM) in CH_3CN were prepared by using excess solid PhIO to optimize yield; after filtration of unreacted PhIO, the solutions represent a reaction system without any methanol or per-acid contaminants. On deaeration of the solutions and a temperature equilibration at 25 °C in the UV–vis cuvette, substrates were added to the stirred solutions. The concentrations of substrates used ranged from 25 to 800 mM and were adjusted to achieve convenient times for the reduction of $\text{Fe}(\text{IV})$ oxo species. The time course decay of the $\text{Fe}(\text{IV})$ oxo was then monitored at 25 °C by the UV–vis spectrophotometer. Time courses were subjected to pseudo-first-order fit, and second-order rate constants were evaluated from the concentration dependence data.

To isolate the organic products, the solutions after the end of the reaction were passed through a silica column, using ethyl acetate as the eluent, in order to remove the metal complex. The ethyl acetate solutions were then analyzed by GC using a known strength of biphenyl solution as the quantification standard. All the data obtained from these studies were collected in Supporting Information Table S2.

Oxygen-Atom Transfer (OAT) Reactions. The $\text{Fe}(\text{IV})$ oxo solutions were prepared as described before. The solutions were placed in cuvette, and the temperature of the UV–vis instrument was monitored to –30 °C. Then, appropriate amounts of thioanisole substrate were added to the $\text{Fe}(\text{IV})$ oxo solution, and the subsequent decay was monitored. Time courses were subjected to pseudo-first-order fit and second-order rate constants were evaluated from the concentration dependence data.

The products were quantified following the procedure already described. The chirality of the sulfoxide product was not determined.

Computational Details and Modeling. All DFT calculations were carried out with the Gaussian 09 package of programs⁶¹ using the B3LYP hybrid functional. This functional is composed of Becke's three-parameter hybrid exchange functional (B3)⁶² and the correlation functional of Lee, Yang, and Parr (LYP).⁶³ The iron atom was described with the Stuttgart–Dresden effective core potential and SDD basis set,⁶⁴ and the 6-31G(d') basis set⁶⁵ was employed for all remaining atoms.

All reported geometries were fully optimized, and analytical second derivatives were evaluated at each stationary point to determine whether the geometry was an energy minimum (no negative eigenvalues) or a transition structure (one negative eigenvalue). Unscaled vibrational frequencies were used to make zero-point and thermal corrections to the electronic energies. The resulting potential

energies and enthalpies are reported in kcal/mol relative to the specified standard. Standard state corrections were applied to all species to convert concentrations from 1 atm to 1 M according to the treatise of Cramer.⁶⁶ Internal reaction coordinate (IRC) calculations were performed on ³TS³AB³CD and ⁵TS⁵AB⁵CD in order to establish the reactant and product species associated with these transition-state structures. The geometry-optimized structures have been drawn with the JIMP2 molecular visualization and manipulation program.⁶⁷

■ ASSOCIATED CONTENT

■ Supporting Information

ESI-MS, ¹H NMR, and FT-IR spectra of complexes 1·(ClO₄)₂ and 2·(ClO₄)₂; the UV-vis spectra of the ligands; the cyclic voltammetric diagrams of complexes 1·(ClO₄)₂ and 2·(ClO₄)₂; the kinetic absorbance spectra of formation of complexes 3 and 4; HRMS of complexes 3 and 4; detailed product analyses; figures of the optimized ground-state and transition-state structures for the toluene and methane oxidation cycles involving ³E; along with tables of atomic coordinates and electronic energies for all optimized structures. Crystallographic details in CIF format. The Supporting Information is available free of charge on the ACS Publications website at DOI: 10.1021/ic5029564.

■ AUTHOR INFORMATION

Corresponding Author

*E-mail: Ebbe.Nordlander@chemphys.lu.se.

Notes

The authors declare no competing financial interest.

■ ACKNOWLEDGMENTS

This research has been carried out within the framework of the International Research Training Group *Metal Sites in Biomolecules: Structures, Regulation and Mechanisms* (www.biometals.eu) and has also been supported by COST Action CM1003. M.M. thanks the European Union for an Erasmus Mundus fellowship. M.G.R. thanks the Robert A. Welch Foundation (Grant B-1093) and the Wenner-Gren Foundation for financial support and acknowledges computational resources through UNT's High Performance Computing Services funded by NSF (CHE-0741936).

■ REFERENCES

- (1) (a) Costas, M.; Mehn, M. P.; Jensen, M. P.; Que, L., Jr. *Chem. Rev.* **2004**, *104*, 939–986. (b) Abu-Omar, M. M.; Loaiza, A.; Hontzeas, N. *Chem. Rev.* **2005**, *105*, 2227–2252. (c) Shan, X. P.; Que, L., Jr. *J. Inorg. Biochem.* **2006**, *100*, 421–433. (d) Kryatov, S. V.; Rybak-Akimova, E. V.; Schindler, S. *Chem. Rev.* **2005**, *105*, 2175–2226. (e) Bruijninx, P. C. A.; van Koten, G.; Klein Gebbink, R. J. M. *Chem. Soc. Rev.* **2008**, *37*, 2716–2744. (f) Meunier, B.; de Visser, S. P.; Shaik, S. *Chem. Rev.* **2004**, *104*, 3947–3980.
- (2) McDonald, A. R.; Que, L., Jr. *Coord. Chem. Rev.* **2013**, *257*, 414–428.
- (3) (a) Kovaleva, E. G.; Lipscomb, J. D. *Nat. Chem. Biol.* **2008**, *4*, 186–193. (b) Groves, J. T. *J. Inorg. Biochem.* **2006**, *100*, 434–447.
- (4) (a) Bollinger, J. M., Jr.; Price, J. C.; Hoffart, L. M.; Barr, E. W.; Krebs, C. *Eur. J. Inorg. Chem.* **2005**, *2005*, 4245–4254. (b) Price, J. C.; Barr, E. W.; Tirupati, B.; Bollinger, J. M., Jr.; Krebs, C. *Biochemistry* **2003**, *42*, 7497–7508.
- (5) Hoffart, L. M.; Barr, E. W.; Guyer, R. B.; Bollinger, J. M., Jr.; Krebs, C. *Proc. Natl. Acad. Sci. U. S. A.* **2006**, *103*, 14738–14743.
- (6) Galonic, D. P.; Barr, E. W.; Walsh, C. T.; Bollinger, J. M., Jr.; Krebs, C. *Nat. Chem. Biol.* **2007**, *3*, 113–116.

(7) Eser, B. E.; Barr, E. W.; Frantom, P. A.; Saleh, L.; Bollinger, J. M., Jr.; Krebs, C.; Fitzpatrick, P. F. *J. Am. Chem. Soc.* **2007**, *129*, 11334–11335.

(8) Matthews, M. L.; Krest, C. M.; Barr, E. W.; Vaillancourt, F. H.; Walsh, C. T.; Green, M. T.; Krebs, C.; Bollinger, J. M., Jr. *Biochemistry* **2009**, *48*, 4331–4343.

(9) (a) Krebs, C.; Fujimori, D. G.; Walsh, C. T.; Bollinger, J. M., Jr. *Acc. Chem. Res.* **2007**, *40*, 484–492. (b) Proshlyakov, D. A.; Henshaw, T. F.; Monterosso, G. R.; Ryle, M. J.; Hausinger, R. P. *J. Am. Chem. Soc.* **2004**, *126*, 1022–1023.

(10) (a) Nam, W. *Acc. Chem. Res.* **2007**, *40*, 522–531. (b) Que, L., Jr. *Acc. Chem. Res.* **2007**, *40*, 493–500. (c) Lyakin, Y. O.; Shteinman, A. A. *Kinet. Catal.* **2012**, *53*, 694–713.

(11) Hohenberger, J.; Ray, K.; Meyer, K. *Nat. Commun.* **2012**, *3*, 720–733.

(12) Sastri, C. V.; Lee, J.; Oh, K.; Lee, Y. J.; Lee, J.; Jackson, T. A.; Ray, K.; Hirao, H.; Shin, W.; Halfen, J. A.; Kim, J.; Que, L., Jr.; Shaik, S.; Nam, W. *Proc. Natl. Acad. Sci. U. S. A.* **2007**, *104*, 19181–19186.

(13) Kaizer, J.; Klinker, E. J.; Oh, N. Y.; Rohde, J. U.; Song, W. J.; Stubna, A.; Kim, J.; Munck, E.; Nam, W.; Que, L., Jr. *J. Am. Chem. Soc.* **2004**, *126*, 472–473.

(14) (a) Hirao, H.; Que, L., Jr.; Nam, W.; Shaik, S. *Chem. - Eur. J.* **2008**, *14*, 1740–1756. (b) Hirao, H.; Kumar, D.; Que, L., Jr.; Shaik, S. *J. Am. Chem. Soc.* **2006**, *128*, 8590–8606. (c) Cho, K. B.; Shaik, S.; Nam, W. *Chem. Commun.* **2010**, *46*, 4511–4513. (d) Kumar, D.; Hirao, H.; Que, L., Jr.; Shaik, S. *J. Am. Chem. Soc.* **2005**, *127*, 8026–8027. (e) Hirao, H.; Kumar, D.; Thiel, W.; Shaik, S. *J. Am. Chem. Soc.* **2005**, *127*, 13007–13018. (f) Bernasconi, L.; Louwse, M. J.; Baerends, E. J. *Eur. J. Inorg. Chem.* **2006**, *2007*, 3023–3033. (g) Janardanan, D.; Wang, Y.; Schyman, P.; Que, L., Jr.; Shaik, S. *Angew. Chem., Int. Ed.* **2010**, *49*, 3342–3345. (h) Chen, H.; Lai, W.; Shaik, S. *J. Phys. Chem. Lett.* **2010**, *1*, 1533–1540. (i) Geng, C.; Ye, S.; Neese, F. *Angew. Chem., Int. Ed.* **2010**, *49*, 5717–5720. (j) Ye, S.; Neese, F. *Curr. Opin. Chem. Biol.* **2009**, *13*, 89–99. (k) Godfrey, E.; Porro, C. S.; de Visser, S. P. *J. Phys. Chem. A* **2008**, *112*, 2464–2468. (l) de Visser, S. P.; Oh, K.; Han, A. R.; Nam, W. *Inorg. Chem.* **2007**, *46*, 4632–4641. (m) de Visser, S. P.; Latifi, R.; Tahsini, L.; Nam, W. *Chem. - Asian J.* **2011**, *6*, 493–504.

(15) Seo, M. S.; Kim, N. H.; Cho, K. B.; So, J. E.; Park, S. K.; Clemancey, M.; Garcia-Serres, R.; Latour, J. M.; Shaik, S.; Nam, W. *Chem. Sci.* **2011**, *2*, 1039–1045.

(16) England, J.; Martinho, M.; Farquhar, E. R.; Frisch, J. R.; Bominaar, E. L.; Munck, E.; Que, L., Jr. *Angew. Chem., Int. Ed.* **2009**, *48*, 3622–3626.

(17) Macbeth, C. E.; Golombek, A. P.; Young, V. G., Jr.; Yang, C.; Kuczera, K.; Hendrich, M. P.; Borovik, A. S. *Science* **2000**, *289*, 938–941.

(18) Wang, D.; Ray, K.; Collins, M. J.; Farquhar, E. R.; Frisch, J. R.; Gomez, L.; Jackson, T. A.; Kerschner, M.; Waleska, A.; Comba, P.; Costas, M.; Que, L., Jr. *Chem. Sci.* **2013**, *4*, 282–291.

(19) Bigi, J. P.; Harman, W. H.; Lassalle-Kaiser, B.; Robles, D. M.; Stich, T. A.; Yano, J.; Britt, R. D.; Chang, C. J. *J. Am. Chem. Soc.* **2012**, *134*, 1536–1542.

(20) England, J.; Guo, Y.; Van Heuvelen, K. M.; Cranswick, M. A.; Rohde, G. T.; Bominaar, E. L.; Munck, E.; Que, L., Jr. *J. Am. Chem. Soc.* **2011**, *133*, 11880–11883.

(21) Biswas, A. N.; Puri, M.; Meier, K. K.; Oloo, W. N.; Rohde, G. T.; Bominaar, E. L.; Munck, E.; Que, L., Jr. *J. Am. Chem. Soc.* **2015**, *137*, 2428–2431.

(22) Lubben, M.; Meetsma, A.; Wilkinson, E. C.; Feringa, B. L.; Que, L., Jr. *Angew. Chem., Int. Ed. Engl.* **1995**, *34*, 1512–1514.

(23) Klinker, E. J.; Kaizer, J.; Brennessel, W. W.; Woodrum, N. L.; Cramer, C. J.; Que, L., Jr. *Angew. Chem., Int. Ed.* **2005**, *44*, 3690–3694.

(24) (a) McQuilken, A. C.; Jiang, Y.; Siegler, M. A.; Goldberg, D. P. *J. Am. Chem. Soc.* **2012**, *134*, 8758–8761. (b) Sahu, S.; Widger, L. R.; Quesne, M. G.; de Visser, S. P.; Matsumura, H.; Moenne-Loccoz, P.; Siegler, M. A.; Goldberg, D. P. *J. Am. Chem. Soc.* **2013**, *135*, 10590–10593. (c) Widger, L. R.; Davies, C. G.; Yang, T.; Siegler, M. A.

- Troepner, O.; Jameson, G. N. L.; Ivanovic-Burmazovic, I.; Goldberg, D. P. *J. Am. Chem. Soc.* **2014**, *136*, 2699–2702.
- (25) Draksharapu, A.; Li, Q.; Logtenberg, H.; van den Berg, T. A.; Meetsma, A.; Killen, J. S.; Feringa, B. L.; Hage, R.; Roelfes, G.; Browne, W. R. *Inorg. Chem.* **2012**, *51*, 900–913.
- (26) Wang, B.; Wang, S.; Xia, C.; Sun, W. *Chem. - Eur. J.* **2012**, *18*, 7332–7335.
- (27) Mitra, M.; Lloret-Fillol, J.; Haukka, M.; Costas, M.; Nordlander, E. *Chem. Commun.* **2014**, *50*, 1408–1410.
- (28) (a) Goodgame, M.; Cotton, F. A. *J. Am. Chem. Soc.* **1992**, *84*, 1543–1548. (b) Johnson, C. R.; Shepherd, R. E. *Inorg. Chem.* **1983**, *22*, 3506–3513. (c) Goodgame, D. M. L.; Goodgame, M.; Weeks, M. *J. J. Chem. Soc.* **1964**, 5194–5199.
- (29) Roelfes, G.; Branum, M. E.; Wang, L.; Que, L., Jr.; Feringa, B. L. *J. Am. Chem. Soc.* **2000**, *122*, 11517–11518.
- (30) Niemers, E.; Hiltmann, R. *Synthesis* **1976**, 1976, 593–595.
- (31) Roelfes, G.; Lubben, M.; Chen, K.; Ho, R. Y. N.; Meetsma, A.; Genseberger, S.; Hermant, R. M.; Hage, R.; Mandal, S. K.; Young, V. G., Jr.; Zang, Y.; Kooijman, H.; Spek, A. L.; Que, L., Jr.; Feringa, B. L. *Inorg. Chem.* **1999**, *38*, 1929–1936.
- (32) Patra, A. K.; Olmstead, M. M.; Mascharak, P. K. *Inorg. Chem.* **2002**, *41*, 5403–5409.
- (33) Wong, E.; Jeck, J.; Grau, M.; White, A. J. P.; Britovsek, G. J. P. *Catal. Sci. Technol.* **2013**, *3*, 1116–1122.
- (34) (a) Decker, A.; Rohde, J.-U.; Que, L., Jr.; Solomon, E. *J. Am. Chem. Soc.* **2004**, *126*, 5378–5379. (b) Decker, A.; Rohde, J.-U.; Klinker, E. J.; Wong, S. D.; Que, L., Jr.; Solomon, E. I. *J. Am. Chem. Soc.* **2007**, *129*, 15983–15996.
- (35) Assuming an idealized C_{4v} symmetry, the band may be attributed to a d–d transition(s) where the excited state is localized in the x - y plane and is related to the equatorial ligand field. This has been shown for the complex $[\text{Fe}^{\text{IV}}(\text{O})(\text{TMC})(\text{NCMe})]^{2+}$, which has a closely related optical spectrum (see ref 34b).
- (36) McDonald, A. R.; Guo, Y.; Vu, V. V.; Bominaar, E. L.; Munck, E.; Que, L., Jr. *Chem. Sci.* **2012**, *3*, 1680–1693.
- (37) Thibon, A.; England, J.; Martinho, M.; Young, V. G.; Frisch, J. R.; Guillot, R.; Girerd, J.-J.; Munck, E.; Que, L., Jr.; Banse, F. *Angew. Chem., Int. Ed.* **2008**, *47*, 7064–7067.
- (38) England, J.; Bigelow, J. O.; Van Heuvelen, K. M.; Farquhar, E. R.; Martinho, M.; Meier, K. K.; Frisch, J. R.; Munck, E.; Que, L., Jr. *Chem. Sci.* **2014**, *5*, 1204–1215.
- (39) Bukowski, M. R.; Comba, P.; Lienke, A.; Limberg, C.; Laorden, C. L. D.; Mas-Balleste, R.; Murz, M.; Que, L., Jr. *Angew. Chem., Int. Ed.* **2006**, *45*, 3446–3449.
- (40) Company, A.; Sabenya, G.; Gonzalez-Bejar, M.; Gomez, L.; Clemancey, M.; Blondin, G.; Jasniewski, A. J.; Puri, M.; Browne, W. R.; Latour, J. M.; Que, L., Jr.; Costas, M.; Perez-Prieto, J.; Lloret-Fillol, J. *J. Am. Chem. Soc.* **2014**, *136*, 4624–4633.
- (41) Klinker, E. J.; Shaik, S.; Hirao, H.; Que, L., Jr. *Angew. Chem., Int. Ed.* **2009**, *48*, 1291–1295.
- (42) Borovik, A. S. *Chem. Soc. Rev.* **2011**, *40*, 1870–1874.
- (43) Bell, R. P. *Proc. R. Soc. London, Ser. A* **1936**, *154*, 414–429.
- (44) Evans, M. G.; Polanyi, M. *Trans. Faraday Soc.* **1938**, *34*, 11–24.
- (45) (a) Mayer, J. M. *Acc. Chem. Res.* **1998**, *31*, 441–450. (b) Warren, J. J.; Tronic, T. A.; Mayer, J. M. *Chem. Rev.* **2010**, *110*, 6961–7001. (c) Mayer, J. M. *Acc. Chem. Res.* **2011**, *44*, 36–46.
- (46) Shaik, S.; Chen, H.; Janardanan, D. *Nat. Chem.* **2011**, *3*, 19–27.
- (47) Wong, S. D.; Bell, C. B., III; Liu, L. V.; Kwak, Y.; England, J.; Alp, E. E.; Zhao, J.; Que, L., Jr.; Solomon, E. I. *Angew. Chem., Int. Ed.* **2011**, *50*, 3215–3218.
- (48) Janardanan, D.; Usharani, D.; Chen, H.; Shaik, S. *J. Phys. Chem. Lett.* **2011**, *2*, 2610–2617.
- (49) Usharani, D.; Janardanan, D.; Shaik, S. *J. Am. Chem. Soc.* **2011**, *133*, 176–179.
- (50) The DFT-optimized structures for all species on the triplet π and quintet σ surfaces have been deposited as [Supporting Information](#).
- (51) (a) We have also probed the activation of methane via a quintet π manifold and find this H-abstraction to lie ca. 7 kcal/mol higher in energy than ${}^3\text{TS}^3\text{AB}^3\text{CD}$ in excellent agreement with the recent review by Shaik et al. on related systems. (b) Usharani, D.; Janardanan, D.; Li, C.; Shaik, S. *Acc. Chem. Res.* **2013**, *46*, 471–482.
- (52) (a) Shaik, S.; Lai, W.; Chen, H.; Wang, Y. *Acc. Chem. Res.* **2010**, *43*, 1154–1165. (b) Ye, S.; Geng, C. Y.; Shaik, S.; Neese, F. *Phys. Chem. Chem. Phys.* **2013**, *15*, 8017–8030.
- (53) Zhou, Y.; Shan, X.; Mas-Balleste, R.; Bukowski, M. R.; Stubna, A.; Chakrabarti, M.; Slominski, L.; Halfen, J. A.; Munck, E.; Que, L., Jr. *Angew. Chem., Int. Ed.* **2008**, *47*, 1896–1899.
- (54) Amrutkar, S. V.; Bhagat, U. D.; Pargharmol, P.; Kotgire, S. S.; Ranawat, M. S. *Int. J. Pharm. Pharm. Sci.* **2010**, *2*, 84–92.
- (55) *APEX2—Software Suite for Crystallographic Programs*; Bruker AXS, Inc.: Madison, WI, 2009.
- (56) Sheldrick, G. M. *Acta Crystallogr., Sect. A: Found. Crystallogr.* **2008**, *A64*, 112–122.
- (57) Farrugia, L. J. *J. Appl. Crystallogr.* **1999**, *32*, 837–837.
- (58) Spek, A. L. *J. Appl. Crystallogr.* **2003**, *36*, 7–13.
- (59) Sheldrick, G. M. *SADABS, Bruker AXS Scaling and Absorption Correction*; Bruker AXS, Inc.: Madison, WI, 2008.
- (60) Sheldrick, G. M. *SHELXTL, Bruker Analytical X-ray Systems*; Bruker AXS, Inc.: Madison, WI, 2005.
- (61) Frisch, M. J.; et al. *Gaussian 09, Revision E.01*; Gaussian, Inc.: Wallingford, CT, 2009.
- (62) Becke, A. D. *J. Chem. Phys.* **1993**, *98*, 5648–5652.
- (63) Lee, C.; Yang, W.; Parr, R. G. *Phys. Rev. B: Condens. Matter Mater. Phys.* **1988**, *37*, 785–789.
- (64) (a) Dolg, M.; Wedig, U.; Stoll, H.; Preuss, H. *J. Chem. Phys.* **1987**, *86*, 866. (b) Walch, S. P.; Bauschlicher, C. W. *J. Chem. Phys.* **1983**, *78*, 4597–4605.
- (65) (a) Petersson, G. A.; Bennett, A.; Tensfeldt, T. G.; Al-Laham, M. A.; Shirley, W. A.; Mantzaris, J. *J. Chem. Phys.* **1988**, *89*, 2193–2218. (b) Petersson, G. A.; Al-Laham, M. A. *J. Chem. Phys.* **1991**, *94*, 6081–6090.
- (66) Cramer, C. J. *Essentials of Computational Chemistry*, 2nd ed.; Wiley: Chichester, U.K., 2004.
- (67) *JIMP2, version 0.091*, a free program for the visualization and manipulation of molecules: (a) Hall, M. B.; Fenske, R. F. *Inorg. Chem.* **1972**, *11*, 768–775. (b) Manson, J.; Webster, C. E.; Hall, M. B. Texas A&M University, College Station, TX, 2006; <http://www.chem.tamu.edu/jimp2/index.html>.